UNIVERSITY OF CALIFORNIA, SAN DIEGO

Sequestration of terrigenous organic carbon on the northern California shelf: the role of hyperpycnal flows

A Thesis submitted in partial satisfaction of the requirements
for the degree Master of Science

in

Earth Sciences

by

Raphaële E. Moeremans

Committee in Charge:

Professor Neal Driscoll, Chair
Professor Miriam Kastner
Professor Lisa Tauxe

2011

The Thesis of Raphaële E. Moeremans is approved, and it is acceptable in quality and form for publication on microfilm and electronically:

_____

_____

_____

Chair

University of California, San Diego

2011

TABLE OF CONTENTS

ACKNOWLEDGEMENTS

I would like to thank my advisor, Prof. Neal Driscoll, for his encouragement and support throughout my research and for enthusiastically sharing his great knowledge, from the early stages of my student career to the final moments of writing this thesis.

I would also like to sincerely thank Prof. Miriam Kastner and Prof. Lisa Tauxe for their guidance and insightful comments. I am grateful for Prof. Miriam Kastner's essential input regarding the geochemical part of this project and for Prof. Lisa Tauxe's valuable advice since the early stages of my research.

I also thank all those who supported me in any aspect, knowingly or unknowingly, throughout the completion of my degree.

LIST OF FIGURES

LIST OF TABLES

ABSTRACT OF THE THESIS

Sequestration of terrigenous organic carbon on the northern California shelf: the role of hyperpycnal flows

by

Raphaële E. Moeremans

Master of Science in Earth Sciences

University of California, San Diego, 2011

Professor Neal Driscoll, Chair

Mountainous rivers that drain active continental margins deliver a significant fraction of particulate organic carbon (POC) to the oceans, which makes such river systems a key component of the global carbon cycle. Understanding the fate of terrigenous organic carbon in the ocean is important for quantifying ocean carbon budgets over long periods of time. This research

gives insight on the fate of POC in active continental margins, such as the Eel River margin. The Eel River margin has such a narrow shelf (10-20 kilometers) and high suspended sediment concentration (>40g/L) during flood events that a large fraction of terrigenous sediment is dispersed by hyperpycnal flows (river density greater than ocean density) and bypasses the shelf. Three piston cores were acquired on the Humboldt Slide and one piston core was taken away from the site, serving as a control. The geochemical signature of the POC layers present in the cores was determined using an Avaatech x-ray fluorescence (XRF) core scanner. The downcore elemental profiles were also used to study the sedimentation history on the Humboldt Slide. Mechanisms identified as controlling sedimentary processes on the Eel River margin and resulting in the sequestration of terrigenous organic carbon in the ocean are earthquake and precipitation-induced landslides as well as storm-driven fluvial discharge.

1. Introduction: the project and its goal

This thesis presents an analysis, which, on the one hand, aims at understanding the processes that lead to the preservation of terrigenous organic carbon on the continental margin and, on the other hand, attempts to investigate the role of climate variability in the sequestration of organic carbon on the continental margin. Sequestration of organic carbon on the margin is important for the quantification of carbon budgets over geological time and for the generation of methane gas. To achieve this goal, piston cores acquired on the Eel margin were geochemically analyzed using XRF data. The obtained XRF data is used to bring a new perspective and complement previous research in the objective to better understand the processes that lead to the deposition of terrigenous organic matter on the continental slope.

Estimates predict that over 10 gigatons of sediment, or half of the global sediment budget of 20 gigatons per year, are discharged into the ocean from small mountainous rivers each year, most of which drain basins that border the Pacific Ocean (Milliman et al., 1983, Milliman & Syvitski, 1992). A few large river systems, such as the Amazon or the Ganges, are responsible for the rest of the global sediment budget (Milliman et al., 1983, Milliman & Syvitski, 1992). Additionally, significant amounts of terrestrial organic carbon may deposit and accumulate in continental margin depocenters, for long periods of time. Active

margin drainage systems that are wave-dominated like the Eel River have small estuaries and narrow deltas, unlike tide-dominated systems such as the Fly River (Harris et al., 1993). In active margin systems, the organic matter is transported and deposited at high rates with little to no subsequent reworking and oxidation (Schwehr et al., 2007). Particulate Organic Carbon (POC) layers in the sediment are of interest because they could mark the occurrence of winter storm events, which deliver sediment and biomass to the ocean.

The Eel River is a storm-dominated environment with a high sediment yield. During storm events, organic terrigenous sediment bypasses the shelf and is rapidly deposited on the slope as dark, coarse-grained layers. A geochemical analysis of sediment cores acquired on the Eel margin will allow to determine the geochemical signature of these layers and to better understand the mechanisms that result in their deposition. The deposition of such organic layers is important for the long-term carbon budget and for methane gas generation.

Three long piston cores from the Eel margin, northern California, spanning close to the last five thousand years have been studied using the Avaatech XRF core scanner to measure downcore elemental profiles. The elements Ba, Ti, Fe, Ca, Sr, S, and Si were measured, as well as some of their ratios. Titanium and iron are used as proxies for the riverine input of terrestrial material (Haug et al., 2001). Barium is associated with the presence of organic matter (McManus et al.,

1998, Paytan et al., 1996, Pfeifer et al., 2001). Sulfur is also high in organic-rich sediments (Berner and Raiswell, 1983). Strontium is associated with continental weathering and calcium with pelagic deposition (Croudace et al., 2006, Ingram et al., 1992).

XRF is a useful method of sediment core analysis because it provides high-resolution data that can be used for a multitude of applications, including the study of changes in paleoenvironmental conditions, sediment deposition patterns, and more.

The presence of terrigenous organic carbon layers in the cores is recurring and could be associated with known patterns of climate variability such as the Pacific Decadal Oscillation (PDO). Hyperpycnal flows, which occur as the river density is greater than the ocean density, when river discharge is heavily loaded with suspended sediment (Warrick & Milliman, 2003), are an important process that leads to the sequestration of terrestrial organic carbon in the ocean. Downcore x-ray fluorescence data will help us investigate the geochemical signature of these flows.

The interest of this project is twofold: to determine the geochemical signature of the terrigenous layers deposited by gravity flows and to investigate the role of climatic variability, particularly the Pacific Decadal Oscillation, in the

sequestration of organic carbon on the northern California margin over the last 5000 years. In addition, a correlation between cores PC01, PC02, and PC07, using geochemical data, is proposed in order to evaluate, from a new perspective, the correlation previously established using grain size data and radiocarbon dating (McCullough, 2008).

Northern California, including the Eel River basin, is an ideal site to study the transport of terrestrial sediment to the continental slope because of large rainfall events in the region, its weak and unconsolidated sedimentary rocks, and steep topography intensifying erosion rates. The modern Eel River drains a coastal region undergoing uplift and high rainfall (Burger et al., 2001, Sommerfield & Nittrouer, 1997, Spinelli & Field, 2003). All these conditions result in exceptionally high sediment yield. Additionally, the shelf is very narrow, only 20 kilometers wide, allowing the sediment to easily bypass it and be deposited on the slope (Burger et al., 2001, Sommerfield & Nittrouer, 1997, Spinelli & Field, 2003, Warrick & Milliman, 2003). Moreover, large amounts of data about sedimentation on the northern California continental shelf are available as the result of extensive research that took place in the context of the STRATA FORmation on Margins (STRATAFORM) projects, initiated in 1994. A primary goal of the project was to study how modern sediment transport processes influence the formation of the long-term stratigraphic record on continental margins (Nittrouer, 1998, Walsh & Nittrouer, 1998). Furthermore, the

STRATAFORM project aims at investigating depositional and erosional processes on the continental margin of northern California, at various temporal and spatial scales. As a result, an abundance of data is available to investigate topics ranging from modern sediment dispersal to the formation of strata over short time-scales, to the long-term preservation of stratigraphy, providing a solid background for this research.

This thesis is composed of three main parts. The first part provides context for this research project by describing the geological setting of the area of interest, as well as data obtained from previous studies on the cores. The second part describes the methodology followed to conduct this research, particularly the processing of XRF data and the presentation of the various geochemical proxies used. The third part offers the results of the research project, with descriptions of the data as well as an interpretation.

2. Contextualization

Two main topics are addressed in this section: the geological context of the Eel River, as well as a summary of previous studies completed with the cores.

2.1. Geological Setting

The tectonic environment of the Eel River results in a high transport of terrestrial sediment to the continental slope. The Eel River has a high sediment yield and the river discharge of the Eel River is highly episodic and storm-dominated. The rapid deposition of terrigenous organic matter on the continental slope results in dark POC layers identifiable in the cores. The geochemical analysis completed for this research mainly focuses on these flood layers.

2.1.1 Tectonic Environment

The Eel River is located in a fore-arc basin, which began to form during the Miocene (Burger et al., 2001). The Eel Canyon cuts the Eel Shelf, southwest of the Eel River mouth. The Eel margin trends NNE-SSW.

The Eel River basin extends for approximately 210 kilometers long, having its northern boundary at Cape Sebastian in Oregon and its southern end at Cape

Mendocino, in northern California (Figure 1). To the west, the Eel River basin is bordered by the Cascadia subduction zone and by the Mendocino Fracture Zone to the south. The Eel River basin undergoes east-northeast compression, due to the convergence of the Gorda plate and the North American plate, and is also influenced by the northward migration of the Mendocino Triple Junction. Due to this northward migration of the Medocino Triple Junction and to northwest translation of the Sierra Nevada, the southern portion of the basin margin is being uplifted at quite high rates (2.8 mm/yr) (Burger et al., 2001). High slopes combined with large precipitation events lead to rapid onshore erosion and large sediment discharge.

Northern California, in general, and the Eel River more particularly, is an excellent location to observe and study the transport of terrestrial sediment to the continental slope. Indeed, the exceptionally high sediment yield in the Eel River basin is a result of several factors related to its location. Firstly, the Eel River drains a coastal area that experiences heavy rainfall events, particularly during the winter months (Sommerfield & Nittrouer, 1997). Also, the Eel River traverses the Mendocino Range, which is mainly constituted of Cretaceaous deep-water sedimentary rocks and the weak metamorphic and mafic volcanic rocks of the Franciscan Formation (altered mafic volcanic rocks, chert, limestones, sandstones, shales, and high pressure metamorphic rocks). Finally, the steep topography of the area, due to uplift, intensifies erosion. Uplift rates in the

drainage basin of the Eel River are high, resulting in the exposure of subsurface rocks (Burger et al., 2001, Sommerfield & Nittrouer, 1997, Spinelli & Field, 2003).

The combination of topograpgy, heavy rainfall events, and the nature of the Franciscan Formation, induces a sediment contribution of about 16 million tons to the basin, annually (Sommerfield & Nittrouer, 1997). The entire basin experienced faulting and folding caused by the underthrusting of the Gorda plate, the southern part of the Juan de Fuca plate, under the North American plate.

2.1.2 Sediment Budget and Accumulation

Most of the sedimentation on the Eel margin is dominated by short-term processes particularly flood events, which result in gravity flows that bypass the continental shelf.

Tectonically active continental margins have a high sediment transport to the ocean because of high topography and flood events (Milliman & Meade, 1983, Milliman & Syvitski, 1992). The Eel River supplies the largest amount of sediment to the California margin, relative to its drainage basin area of 8640 km^2. The mean annual suspended sediment-load ranges between 14 and 23 x 10^6 tons per year (Sommerfield & Nittrouer, 1997). As mentioned earlier, the rugged terrain surrounding the Eel River drainage basin, with maximum altitudes between 1500 and 2000 meters, results in a high sediment yield (Sommerfield & Nittrouer, 1997).

Most of the river discharge, about 90 percent, happens in the winter months, between November and May, in response to large storm events. Extremely turbid flows usually follow storm events. The results of Sommerfield et al. (1997) and Wheatcroft et al. (1997) studies show that sedimentation on long time scales can be controlled by short-term sediment processes associated with flood events. In addition, the results demonstrate that a large portion of sediments supplied by flood-dominated mountainous rivers to tectonically active margins bypasses the narrow continental shelves (Sommerfield & Nittrouer, 1997).

Studies regarding the modern accumulation rates, sediment budget, and depositional environment show that 25% of the total suspended load of the Eel River is composed of fine sands, which are deposited on the inner shelf and are subject to reworking by large wave and littoral transport (Sommerfield & Nittrouer, 1997).

Short-term processes of sediment transport have been observed and documented in order to provide a conceptual understanding of the mechanisms that lead to sediment delivery to the continental slope (Walsh & Nittrouer, 1998).

Deposition on the continental slope results from hyperpycnal plumes produced from the flood-event-dominated Eel River discharge, which are capable

of traveling along the seafloor over great distances past the shelf. According to buoyancy theory, the hyperpycnal threshold for southern California rivers is of 1040kg/m^3 with an average ocean density of 1025kg/m^3 (Warrick & Milliman, 2003). The Humboldt Slide deposit is thought to record primary deposition as a result of hyperpycnal flows, as it has undergone little or no post-depositional deformation.

A strongly coherent relationship between river discharge and precipitation has also been documented for storm events in the Eel River basin (Wheatcroft et al., 1997). Large storm events, resulting in high discharge, lead to the delivery of large amounts of sediment to the ocean. This coherent relationship between precipitation and river discharge results in turbid waters that create hyperpycnal flows when entering the ocean.

Hyperpycnal flows are capable of transporting terrestrial organic matter past the continental shelf (Wheatcroft et al., 1997). Flood layers, which are geochemically and sedimentologically distinct from the underlying sediments, were shown to represent only about 25 percent of the flood load. Indeed, the study shows that 75 percent of the flood-derived sediment did not form a recognizable deposit but was deposited rapidly and widely across the continental margin, due to wave resuspension and currents.

Sedimentation is episodic and is controlled principally by storm-generated flood plumes. Modern sedimentation rates on the shelf range between 2 and 14 millimeters per year (Sommerfield and Nittrouer, 1999). During recent flood events, southerly winds have dominated, resulting in sediments being deposited north of the Eel River mouth (Burger et al., 2001). Seaward transport of sediment is also important. Recent studies have shown that as much as 75 percent of the sediment discharged to the 15 kilometers-wide shelf bypasses it and is preserved on the upper slope (Wheatcroft et al., 1997).

Sediment fluxes on the continental slope, off the Eel River, have been observed using time-series sediment traps over a period between September 1995 and January 1997 (Walsh and Nittrouer, 1999). The sediment-trap samples were then analyzed for total mass, calcium carbonate, biogenic silica, and total combustible matter. From these data, lithogenic fluxes were determined. The calculated lithogenic fluxes were 53 percent at the top trap, 70 percent in the middle, and 83 percent at the bottom traps. Fluxes of combustible matter and fluxes of calcium carbonate varied similarly to total sediment fluxes. Biogenic silica fluxes behaved more independently and showed little variability. Since lithogenic material constituted the majority of total sediment, about 70 percent, its variations were most closely related with total sediment variations. It was also shown that, typically, sediment fluxes increased with depth (Walsh and Nittrouer, 1999). The major processes that govern sediment supply to the continental slope

include river discharge and biological production. Calcium carbonate and combustible matter varied similarly to lithogenic matter. During the sampling interval of their study, two peaks in sediment discharge are visible in the data. These correspond to the passage of two storm events in December (1996).

In an attempt to understand the sediment deposition from riverine input in coastal zones, which is of major importance in understanding sediment sequences over larger time scales, Morehead and Syvitski (1998) applied a sediment plume model to the Eel margin. Simulations for the Eel river plume were made for present day conditions and 18, 000 years ago, which corresponds to the end of the last glacial maximum. The results from the present day simulation show that majority of the sediment is deposited within 20 kilometers north of the Eel River mouth and 10 kilometers offshore. During a glacial maximum, lower sea level, larger drainage basin, and higher topography results in sediment yields 30 percent higher.

2.1.3. Carbon sequestration

Hyperpycnal flows result in very rapid deposition of layers several centimeters thick of terrigenous material, including a large fraction of organic carbon, as seen in the sediment cores. These high rates of sediment accumulation allow for the terrigenous carbon to be buried at depths where oxidation is either limited or does not occur. Organic layers deposited after a flood are important

areas for methane gas generation, as a result of pyrolysis of this material. Methane gas blowouts are significant factors in slope failures (Driscoll et al., 2000).

Earthquakes and flood generated landslides result in the deposition of layers rich in terrestrial POC and are essential for carbon sequestration. Despite having a carbon yield rate an order of magnitude lower than human induced burial rates, the importance of these processes lie in the fact that they have been occurring over much of the geological time.

Carbon burial and sedimentation on the Eel margin may be controlled in large part by precipitation events and annual and decadal climate variability. Pacific Decadal Oscillation (PDO) imparts an interdecadal variability in the climate of the Pacific Basin, which is recorded in surface winds, sea surface temperature, sea surface pressure (Mantua et al. 1997, Mantua & Hare, 2002). Sea surface temperatures are below average in the central and western North Pacific Ocean and above average in the eastern Pacific, during the warm PDO phase. During cool PDO phases, the opposite conditions occur. The Aleutian low-pressure system is stronger during warm PDO phases and weaker during cool PDO phases (Mantua et al. 1997).

2.2. Piston Cores

During the November 2001 *R/V Thompson* cruise TTN 136B, seven piston cores were acquired in the Eel River basin. The location of the cores sites was based on CHIRP seismic data and bathymetry data (Figures 2 and 3, Table 1). Four out of the seven cores were examined in this study based on their locations: three were recovered in the Humboldt slide (Schwehr et al., 2007), and the other core is north of the slide and farther from the Eel River mouth. The latter core should be less affected by hyperpycnal flow deposition and therefore should not contain recurrent layers of particulate organic carbon. The locations of the core sites were established with an accuracy of about 10 meters, using differential GPS. Core PC01 initially recovered a little less than 8 meters of sediment. During the retrieval, however, a middle portion of the core, subsequently named section 5, was lost (McCullough, 2009). Because the exact length of the lost section is unknown, only the top four sections of core PC01, amounting 508 centimeters of sediment (Figure 4), were used for this study. Cores PC02 and PC07 are 786.5 and 755 centimeters long, respectively (Figures 5 and 6). Core PC05 is 760 centimeters long and is used as a control core (Figure 7). The cores have a diameter of 10.2 centimeters.

Cores PC01, PC02, and PC07 sample a single feature from downslope to upslope. The feature has a wavelength of approximately 150 meters and an

amplitude of about 6 meters. It is located in the center of the Humboldt slide (Figure 3).

TTN136B PC01 is a 10-centimeter diameter piston core (Figure 4) collected from the erosional side of an anti-dune on the Humboldt Slide, Northern California, at 40˚50”20.16’ N and 124˚30”09.96’ W, in 460 meters water depth (Figures 2 and 3). The core is 507 centimeters long and is stored as four sections of 69.5 centimeters, 146 centimeters, 147 centimeters, and 144.5 centimeters long, respectively. The accumulation rates, calculated from radiocarbon dating corrected for reservoir effects, are 0.66 millimeters per year until about 80 centimeters depth, corresponding to an age of 2500 years ago, and 2.14 millimeters per year thereafter. Fifteen POC layers have been identified in this core.

TTN136B PC02, also a 10-centimeter diameter piston core (Figure 5), was collected at the top of an anti-dune on the Humboldt Slide at 40˚50”19.86’ N and 124˚30”07.62’ W, in 460 meters water depth. The core is 778 centimeters long and is stored as seven sections of 60.5 centimeters, 147 centimeters, 149 centimeters, 150 centimeters, 14 centimeters, 117.5 centimeters, and 140 centimeters, respectively (Figures 2 and 3). The fourth section of this core has core cracks and gaps and sections 5 and 6 contain some gaps as well. The accumulation rates are 1.74 millimeters per year until a depth of about 320

centimeters, which corresponds to the same age of 2500 years ago, and 3.60 millimeters per year at greater depths. Seven POC layers have been identified in this core.

TTN136B PC07 (Figure 6) was collected on the upflow side of an anti-dune on the Humboldt Slide at 40˚50”19.87’ N and 124˚30”05.84’ W, in 461 meters water depth (Figures 2 and 3). The core is also 10 centimeters in diameter and 755 centimeters long and is stored as seven sections of 86 centimeters, 94.5 centimeters, 148 centimeters, 150 centimeters, 21 centimeters, 109 centimeters, and 145 centimeters long, respectively. Sections 5 and 6 were scanned together (Figure 24). No dating is available for core PC07 and, consequently, accumulation rates are not known. Five POC layers have been identified in this core.

TTN136B PC05 (Figure 7) was collected away from the Humboldt Slide, at 40˚59”00.30’N and 124˚27”12.08’ W, in 419 meters water depth (Figure 2). The core is 10 centimeters in diameter and 760 centimeters long, stored as six sections of 57 centimeters, 149 centimeters, 149.5 centimeters, 148.5 centimeters, 118 centimeters, and 138 centimeters long, respectively. No radiocarbon dates were acquired for this core either and little to no POC layers are visible.

2.3. Previous Core Analysis

The geochemical analysis of the cores conducted for this project builds on and complements a series of previous core analyses. Anisotropy of magnetic susceptibility (AMS) measurements were made to determine the origin of the features observed in the Humboldt slide (Schwehr et al., 2007). A visual analysis and stratigraphic description, which included a lithographic depiction, sediment color, approximate grain sizes, and the presence of particulate organic carbon, were made for each of the three cores acquired on the Humboldt Slide (McCullough, 2009).

2.3.1. Magnetic Susceptibility

Anisotropy of magnetic susceptibility measurements were done on sediment samples from the cores PC01, PC02, PC05, and PC07. These AMS measurements were made to determine the origin, primary or post-depositional of sedimentary features, observed in the Humboldt slide. The two alternative hypotheses proposed to explain the formation of the Humboldt slide deposit, sediment waves or post-depositional slope failure, would predict different magnetic fabrics. Depositional density current features should display an oblate AMS fabric, while features that have undergone post-depositonal deformation should present triaxial AMS fabric. In order to assess the origin of these features of the Humboldt slide, Schwehr et al. (2007) applied a test based on sedimentary

fabric, as characterized by anisotropy of magnetic susceptibility. AMS fabric can be altered by both mineralogical changes and physical reorientation of the magnetic grains in the sediments.

The data reveals that the top 8 meters of sediment on the Humboldt slide have not experienced post-depositional deformation and suggests that the observed features are formed by primary deposition resulting from downslope density currents, or hyperpycnal flows (Schwehr et al., 2007).

2.3.2. Stratigraphy

A repeating depositional pattern was recognized within all three cores (McCullough, 2009). Distinct coarse-grained packages were identified, often having sharp erosional bases, and separated by layers of normal grading. These packages display fining-upward grain sizes and were up to tens of centimeters thick.

Within the cores are also dark layers that are composed of a large fraction, up to 90 percent, of particulate organic carbon (Figures 4-6). These layers are between a few millimeters to about 10 centimeters thick. Large wood fragments, on the order of a few centimeters, are visible in some of these organic layers. McCullough identified a total of 16, 20, and 11 layers composed of mostly POC in the cores PC01, PC02, and PC07, respectively. Such layers were not observed in

core PC05 (Figure 7). These POC layers are the main focus of the geochemical analysis conducted for the present research.

2.3.3. Grain Size

Samples were collected at the top and base of each of these fining-upward packages as well as at a uniform sampling spacing, in order not to alias the results, and analyzed in order to corroborate that the identified fining-upward packages were characterized by normal grading (McCullough, 2009). They were dried and weighed and subsequently sieved at 63 μm to determine the coarse weight percentage of each sample. The finer portion of each sample was also analyzed in order to construct a grain size spectrum. The visual identification of fining-upward packages observed in the cores was confirmed by grain size data. Fining-upward sequences observed in the cores could also record climate variability, such as shifts between the positive and negative phases of the Pacific Decadal Oscillation.

2.3.4. Age model

The age model of McCullough (2009) provides good temporal constraints on this study. Pelagic and benthic species of foraminifera were collected from the coarse grain fraction of the samples. Additionally, calcareous tests of the forams were picked directly from the cores. Radiocarbon dates obtained from these

marine carbonates were corrected for the effects of both the delay in exchange rates between atmospheric CO_2 and marine HCO_3^- and the mixing of surface waters with old upwelling waters, which are depleted in ^{14}C (Hughen et al., 2004). A correction of 350 years was used (McCullough, 2009).

McCullough (2009) used radiocarbon dates measured from the carbonates and corrected for the previously mentioned reservoir effects to calculate sediment accumulation rates for cores PC01 and PC02 (Figure 8). A significant change in accumulation rates is observed in both cores between 2670 and 2510 years ago. A threefold sedimentation rate increase is observed in core PC01, from 0.66 to 2.14 millimeters per year, and a twofold sedimentation rate increase is observed in core PC02, from 1.74 to 3.6 millimeters per year (McCullough, 2009). Wood fragment samples were not used in the calculation of these sediment accumulation rates, as their residence time in the watershed could introduce much uncertainty.

The accumulation rates, calculated form radiocarbon dates, were used to establish a chronostratigraphy and to date both the fining-upward packages and the POC layers. The base of each layer or package was used to calculate the time of deposition. In the present thesis, the dates and accumulation rates were used to calculate the time recurrence intervals between the POC layers and to reconstruct a sedimentation history for the Humboldt Slide.

2.3.5. Core correlation

Core PC07 was correlated to cores PC01 and PC02 using the largest peak in grain size data (Figure 9, McCullough, 2009). In addition, measured radiocarbon dates were used independently to check the accuracy of the correlation. XRF data from this study is used to establish a corrected correlation between the cores (see section 4.6). Cores PC01 and PC02 overlap between about 3800 and 2400 years. It is visible from the overlapping interval that the number and thickness of fining-upward packages increase landward, with core PC01 having 8 fining-upward packages and core PC02 having 12. This is consistent with the setting of the cores within an anti-dune (seen in Figure 3). Indeed, in an antidune, sediment is deposited on the upstream side and eroded from the downstream side.

The previous studies made on the cores show that the top 8 meters of sediment in the Humboldt Slide have not undergone post-depositional deformation and thus record primary deposition, thus allowing using the geochemistry of the sediments to understand the depositional processes. Also, stratigraphy and grain size analysis have identified fining-upward packages and POC layers within the cores, which are the focus of the geochemical analysis. Finally, radiocarbon dating provides a good age model for the reconstruction of

the depositional history on the Humboldt Slide and the recurrence intervals between the POC layers.

3. Methodology: Processing of the XRF data and choice of proxies

The three piston cores, PC01, PC02, and PC07, acquired on the Humboldt Slide and PC05 were scanned with the XRF core scanner. The XRF data are used to make a corrected correlation between cores, investigate terrigenous sediment input patterns and understanding sedimentation in the Eel Margin. A number of proxies were chosen to determine the geochemical signature of the dark POC layers present in the cores and subsequently understand the processes that lead to their deposition. The selection of the proxies is mainly made in the optic of determining pelagic from terrigenous beds and the presence of organic matter.

3.1. Processing of the XRF data

The cores were scanned using an Avaatech X-ray fluorescence (XRF) core scanner. XRF core scanners allow for rapid collection of high-resolution, continuous, downcore element profiles. In XRF analysis, a beam of incident X-radiation ejects the electrons from inner atomic shells creating vacancies, in which electrons from outer shells fall back (Rothwell & Rack, 2006). The energy difference between inner and outer shell electrons results in surplus energy. This surplus energy, defined here as the difference in energy between vacant inner shells and the outer shells, is in turn emitted as a pulse of X-radiation. The atoms of a specific element emit a characteristic energy and wavelength spectra, which

allow for the recognition and estimation of the element's abundance. In other words, the wavelengths of emitted radiations are distinctive for each element and the amplitude of the peaks in the spectrum are proportional to the concentration of the elements present in the sample (Richter et al., 2006).

The scanner needs to be calibrated. The measurements start automatically after the measurement conditions have been selected. The spectra obtained during scanning are saved and can be viewed in an Excel file as a table with columns recording the number of counts of each detected element at every sample depth. The sample interval for this study is 2 millimeters. The data can then be plotted, using Windows Excel or Matlab, as profiles of number of counts of an element versus downcore depth.

XRF analysis is non-destructive so cores are preserved and can be used for further methods of analysis. XRF core scanning rapidly delivers high-resolution data of the chemical composition of cut sediment cores (Richter et al., 2006). The atomic mass range that can be resolved by the scanner extends from Al to Ba.

The cores were scanned at three energy levels: 10 kV, 30kV, and 50 kV. The first energy level, with a count time of 5 seconds per measurement, detects elements from Al to Rh. The second energy level, with a count time of 20 seconds

per measurement, detects elements from Cu to Bi. The highest energy level, with a count time of 30 seconds per measurement, detects elements from Ag to Ba.

Usually, cores are measured down the center of the split core. However, due to sampling in both the working and archive halves of the core PC05, the track needed to be moved 25 millimeters to one side. This should not affect the data, as the x-rays only penetrate to a superficial depth. The working half of section 1 of core PC05 had to be scanned upside down, since both halves had been over sampled. The data for this section was plotted and flipped in order to display the data normally, with the top of the section up.

Requirements for conventional lab XRF analysis are that the samples be homogenous, dry, and have a flat surface. For the analysis of split sediment core, however, these requirements are never met. The surface of cut cores will present topography and variations in grain size, regardless of how carefully they are cut. For this reason, the core surface is covered with a very thin foil before it is placed in the scanner.

3.2. Proxies

A number of inter-elemental ratios or element integrals were selected to identify characteristic sedimentation features and geochemistry of the various units (Tables 2 and 3). Even though we acknowledge that the measured XRF

element data from the scanner do not have a perfectly constant relationship with the actual element concentration in varying sediment types, a combination of element integrals and ratios can provide substantial information, useful for geochemical interpretation. These include Ba, Ti, Ca, Fe, Si, Sr, S, and their ratios. The ratios are most useful for removing the effects of cracks in the cores, which result in anomalously low counts of the elements, and the effect of reduced number of counts of every element in the POC layers, which are composed of about 90 percent of carbon. For this reason, only ratio plot figures are attached to this document and used for the interpretation of the results.

Identifying genetic sedimentary units and terrigenous units is key to understanding depositional histories and to studying the frequency and, potentially, the control mechanisms on hyperpycnal flows that deliver terrigenous sediment to the continental margin. In marine basins, sedimentary sequences usually comprise an alternation of beds formed either through pelagic and hemipelagic deposition of products derived from biological activity at the surface, or through active sediment transport, mainly sediment hyperpycnal flows and flood event horizons. For distinguishing between sediment beds deposited by hyperpycnal flows from pelagic beds, the presence of sharp erosional bed bases and graded deposits with minimal forams suggests the deposit was emplaced by gravity flows (Rothwell et al., 2006, Rothwell & Rack, 2006). Average sediment accumulation rates are known from radiocarbon dating

of core samples and turbidite emplacement frequency are calculated from the accumulation rates (see Section 4.5).

It is important to note that the sediments in the cores have not experienced diagenesis from deep burial and heating, therefore post-depositional chemical changes should be minimal.

3.2.1. Titanium

Titanium is the ninth most abundant element in the Earth's crust and is present in igneous rocks and sediments derived from them. It is a good proxy for the presence of terrestrial material and has no biological source. Cores from the ODP site 1002, from the Cariaco Basin on the northern shelf of Venezuela, were analyzed with an x-ray fluorescence scanner for iron and titanium and can be used to infer variations in the hydrological cycles with a subdecadal resolution (Haug et al., 2001). Iron variations could be attributed to redox variations in the sediments, while titanium is insensitive to such changes. Variations in titanium can thus be used as a proxy for terrigenous sediment input and can provide a measure for river runoff. Locations nearer to tributaries will be characterized by high contents in titanium, while distal locations will be relatively depleted in Ti. This can be seen in the difference in titanium counts between cores PC01, PC02, and PC07, located close to the Eel River mouth, and PC05, located farther away.

The titanium counts for the three cores located near the Eel River mouth are much higher than those for PC05 (Table 4).

3.2.2. Barium and Ba/Ti ratio

Barium is often used as a geochemical proxy for past and present productivity in the photic zone.

The amount of biogenic barium is estimated by subtracting terrigenous barium from the total barium content present in the sample. Terrigenous barium values are obtained by normalizing with the amount of aluminum or titanium present in the sample and the Ba/Al or Ba/Ti ratio. Several studies have described the link between Barium accumulation in sediments and primary productivity in the photic zone (Goldberg and Arrhenius, 1958; Paytan and Kastner, 1996; Pfeifer et al. 2001; etc). The main carrier of Ba in the water column has been identified to be barite. The formation of barite is thought to be associated with the decay of organic material in the oxygen minimum zone. As a result, a typical water column profile of particulate Barium decreases with depth, having a maximum concentration in the euphotic zone. Other mechanisms responsible for the formation of barite have been discussed in the literature: decaying organic sulfur components, precipitation of organisms that possess skeletons made of barite. The main advantage of using biogenic Barium as a proxy for productivity is the fact that barite is well preserved in sediments. Paytan and Kastner (1996) and Dymond et al. (1992) have conducted studies

investigating the preservation of barite in sediments. Their results point to an average preservation factor of 30 percent.

The amount of barite precipitation is a function of dissolved barium in seawater. The terrigenous barium content of the sediments is estimated based on the concentration of conservative elements like Al or Ti and multiplication with the ratio of either of those in the aluminosilicate fraction to Ba (Pfeifer et al., 2001). Terrigenous Ba/Al or Ba/Ti ratios can be estimated from average crustal value abundances. Despite the fact that most studies described in the literature use aluminum as the conservative terrigenous element, titanium was used as a conservative element for the present study since the measurement of Al counts from XRF is significantly less precise, due to the size of the atom. Indeed, Reitz et al. (2004) have proved that no major difference in conclusion is obtained if Ti is used instead of Al as a terrigenous denominator.

Generally, it was found that a high primary productivity in surface waters corresponds to high biogenic barium accumulation rates in the surface sediments. The use of barium as a proxy for paleoproductivity is, however, based on the assumption that the relation between productivity and sediment accumulation has not varied greatly over time and that the supply, accumulation, and preservation of barite has not changed much either (Paytan et al., 1996). The applicability of this proxy to different settings is, however, still unresolved.

3.2.3. Iron and Fe/Ti ratio

Concentration of iron in surface waters is extremely low (Martin, 1989). The main input of iron into sediments is from terrigenous sources. Fe is prone to diagenic remobilization so normalizing Fe to Ti will highlight the difference between iron that is of terrigenous origin from that associated with redox-related diagenesis. Maxima in Fe/Ti ratio could correspond to the precipitation of pyrite and other sulfide phases. Pyrite (FeS_2, reduced sulfur) has been shown to have a strong positive correlation with organic carbon in modern sediments (Berner & Raiswell, 1983). The oxidation of organic matter results in bacterial sulfate reduction in anoxic sediments. This produces H_2S, which reacts with detrital iron minerals, to form pyrite.

3.2.4. Calcium and Ca/Si ratio

Calcium is a good element to analyze using XRF methods, along with Si, because both elements have high detection. The Ca/Si ratio can be used to determine if sand layers are biogenic, thus enriched in calcium carbonate, versus terrigenous, enriched in silica. Calcium carbonate is the greatest source of sediments, other than river input of eroded material. Very little calcium is present in the rocks of the Franciscan formation that are eroded by the Eel River. It is therefore safe to affirm that peaks in the Ca/Si ratio are mainly associated with the presence of foraminifera and shells.

3.2.5. Strontium and Sr/Ca ratio

Most strontium in the sea is derived from carbonate rocks on continents. Higher Sr count values can thus be related to higher terrigenous input. High Sr/Ca can indicate the dominance of terrigenous input over pelagic deposition.

3.2.6. Sulfur and S/Fe ratio

Sulfur counts are high in organic-rich sediments. Oxygen is rapidly exhausted when organic matter settles on the seafloor. Sulfate is then used by sulfate-reducing prokaryots to oxidize organic matter. Large amounts of sulfide are produced as a result of anaerobic respiration. Changes downcore coincide with limit between oxidizing and reducing environments. S/Fe should reflect sulfide/sulfate abundances. Fe is associated with sulfides, reduced sulfur, such as pyrite and not sulfates, the oxidized form of sulfur, such as barite or gypsum. Decreases in the ratio would indicate higher abundance of sulfides relative to sulfates. Sulfides such as pyrite are strongly correlated with the presence of organic matter.

3.2.7. Silica and Si/Ti ratio

The main sources of silica in sediments are the weathering of rocks and diatoms and, thus, indicate either a terrigenous or productivity source. The Si/Ti

ratio can show the relative contributions of terrigenous-derived silica compared to a biogenic source. Since the sensitivity of the XRF to titanium is strong, the Si/Ti ratio should result in good data.

4. Results

In this section, the processed data is shown and analyzed. Observations of the ratio plots are described for each section. This allowed recognizing a dominant geochemical signature for the terrigenous POC layers and depositional processes that would result in such a signature, as well as the influence of climate variability on these processes.

Finally, correlation between the cores PC01, PC02, and PC07, based on the geochemical data, is proposed in the end of this section.

4.1. Extent of the data set and quality

In addition to the roughness of their surface, cut sediment cores will have downcore variability in composition, water content, texture, and porosity (Rothwell & Rack, 2006). For all these reasons, data acquired using XRF core scanning will be, at best, semi-quantitative. Also, sensitivity decreases with atomic size, due to increased attenuation of the X-rays between the core surface and the detector.

Despite being only semi-quantitative, the results provide reliable records of relative elemental variability. Elemental variations resolved by XRF core scanners are useful for inferring environmental changes and allow discrimination of changes over decadal, annual, or even subannual periods. The effects of surface

roughness and sample heterogeneity increase at higher spatial resolutions. These previously described effects are of less importance in fine-grained sediments, where they are sometimes even negligible. In our case, the resolution used is quite high, 2mm, and coarse grain layers are present in the sediment. For these reasons, the general trends of relative element variability are useful for the interpretation of the data, not every small wiggle in the plots.

The XRF geochemical data are shown in Tables 4 and 5; elemental number of counts are listed in Table 4 and ratio values in Table 5, for each section of the four cores. The tables are divided per core section and show minimum, maximum, and average count values for each element or ratio.

4.2. Analysis of the cores

In this part of the work, observations based on the data plots are presented for each section of the cores. The plots were made in Excel from the data compiled in the output spreadsheets. For each section, all the ratio plots were aligned to the core image in one figure, using Adobe Illustrator. The observations will be synthesized in the next section of this work in order to provide an explanation of the major trends present in the data.

Very little variability in the ratio values, obtained in this study, has been observed in PC01 section 1 (Figure 10). A possible organic rich flood-layer,

highlighted in blue, can be seen, as indicated by the rise in Ba/Ti ratio, Fe/Ti ratio, and S/Fe ratio, at 50-60 mm to 70-80 mm from the top of the section. This layer also displays increases in Ca/Si and Sr/Ca, as well as a low in Si/Ti. A slight hole at 60 mm from the top of the section barely affects the number of counts.

Five organic-rich layers are visible in section 2 of PC01, highlighted in blue (Figure 11). The top layer, from 1376 mm to 1412 mm, is characterized by an increase in Fe/Ti and Sr/Ca ratios, but little to no signal in Ba/Ti, Ca/Si, S/Fe, and Si/Ti ratios. The four other POC layers are characterized by increases in Ba/Ti, Fe/Ti, Ca/Si, and S/Fe and a low in Si/Ti. The second and third layers show an increase in Sr/Ca, while the two last ones show a low in Sr/Ca. These layers are present at the depths of 1538 mm to 1628 mm, 1682 mm to 1718 mm, 2006 mm to 2015 mm, and 2025 mm to 2035 mm.

For section 3 of PC01, five POC layers are observed, at 2370 to 2390 mm, 2470 to 2510 mm, 2570 to 2590 mm, 2850 mm to 2870 mm, and 3450 to 3470 mm (Figure 12). Note that the 50 kV scan failed, resulting in compromised barium data. Despite this, we observe that slight increases in Fe/Ti, Sr/Ca, and S/Fe ratios correspond to the five POC layers, as well as a decrease in Si/Ti. No increases in Ca/Si ratio are observed.

In section 4 of PC01, five POC layers are observed at 3800 to 4050 mm, 4158 to 4180 mm, 4356 to 4378 mm, 4642 mm to 4664 mm, and 4740 to 4752 mm (Figure 13a). The top layer has the general POC layer signature but most of the variability is in Ca/Si, Sr/Ca, and S/Fe and a lot of shell fragments are visible in the core (Figure 13b). The second layer has the typical POC layer signature as well. The third POC layer shows a peak in Ba/Ti ratio but no peaks in Fe/Ti or S/Fe. The second and third layers exhibit signals in Si/Ti. The two bottom layers of this section have lows in Ba/Ti but large peaks in Fe/Ti and S/Fe, as well as small peaks in Ca/Si and Sr/Ca and a slight decrease in Si/Ti.

For section 1 of PC02, there seems to be a POC layer at 561 mm to 580 mm visible in the XRF data, although it is not distinctly visible in the color of the sediments (Figure 14). Some cracks, designated by the letter c in the figures, are visible in this section and result in some low count values for integral profiles but do not necessarily affect the ratio profiles, since low element counts due to the voids cancel out when divided by one another.

One layer is also visible in the bottom of section 2 of PC02, at 2033 to 2050 mm (Figure 15). It has the typical POC layer geochemical signature, with an increase in Ba/Ti, Fe/Ti, Ca/Si, S/Fe, and a drop in Si/Ti. Section 3 of PC02 has no POC layer but does show signs of bioturbation (Figure 16).

The barium scan also failed for section 4 of PC02 but two organic layers are still visible, highlighted in blue (Figure 17). The first one, from 4100 mm to 4300 mm, has a large variability in Sr/Ca ratio but no signal in Ca/Si ratio and very little in the S/Fe ratio. The second POC layer in the section, at 4470 to 4500 mm, has a typical POC layer geochemical signature, with an increase in Ba/Ti, Fe/Ti, Ca/Si, S/Fe, and a drop in Si/Ti. This layer also shows an increase in Sr/Ca.

No POC layers are visible in section 5 of PC02 (Figure 18a, top). Three POC layers, at 5397 mm to 5517 mm, 5677 mm to 5897 mm, and 5977 to 5997 mm are observed in section 6 of PC02 (Figure 18a, bottom). The first and third layers have a typical signature, with an increase in Ba/Ti, Fe/Ti, Ca/Si, S/Fe, and a drop in Si/Ti, while the second one shows a large variability in the Sr/Ca ratio. Larger wood fragments are present in this layer (Figure 18b). A very sharp base layer is present above the wood.

In section 7 of PC02, many cracks are visible (Figure 19). One POC layer is possibly present at 7043 mm to 7065 mm, but it does not have a strong geochemical signal.

Three dark layers are visible in section 1 of PC07, at 169 mm to 193 mm, 361 mm to 385 mm, and 469 mm to 481 mm, with a typical POC layer signature (Figure 20). No POC layers are visible in section 2, but there is evidence for

bioturbation (Figure 21). No POC layers are visible in section 3 of PC07 either, but several shells are present within the sediment (Figure 22a and b).

In section 4 of PC07, between 4301 and 4500 mm, very thin POC layers are visible, with clay beds deposited in between (Figure 23 a and b). This whole package is characterized by a general increase, with high variability, in Ba/Ti, Fe/Ti, Sr/Ca, and Si/Ti. A slight increase is visible in the S/Fe ratio but none in the Ca/Si ratio. Another POC layer is located at about 4600 to 4700 millimeters depth. It is characterized by slight increases in Ba/Ti, Fe/Ti, Sr/Ca, and Si/Ti. No increases in Ca/Si or S/Fe are observed. No dark layers are visible in either section 5 or section 6 of this core (Figure 24).

The geochemistry of PC05 shows very little variability in the ratio and elemental profiles (Figures 25–30). The sediment character of this core looks very similar to the top sections of PC01 and PC02, where few dark layers that are characteristic of the organic layers are visible.

5. Discussion

5.1. Major trends in the profiles

The number of counts for all elements diminishes markedly for the POC layers, composed of about 90% of organic carbon (McCullough, 2009). In order to remove the effect of dilution due to the dominance of carbon in the POC layers, which cause the observed number, ratios of two elements can be employed. The ratio of Fe and Ti can be used as a proxy for the presence of terrestrial and organic material in the sediment. Proxies for the input of terrigenous material, such as Fe/Ti ans Si/Ti, show peaks corresponding to the POC layers. The high Ba/Ti ratios correlate with the emplacement of POC layers within the cores, showing that they are organic-rich layers (Figures 10-30). From the above observation of downcore profiles, a general geochemical signature for the POC flood layers is observed: rises in Ba/Ti, Fe/Ti, and S/Fe ratios and drops in Si/Ti ratios characterize most of the POC layers. Some POC layers show strong variability in Ca/Si ratio or Sr/Ca ratio. This could point to differences in magnitude and duration of flood-events. Terrigenous signatures accompanied with the presence of shells, as in layers observed in PC01 and PC02, could indicate breached watershed dams after large precipitation events, with the discharge lasting through a few tidal cycles. These larger and longer flows would erode the estuary.

Core PC05, located away from the Humboldt Slide, at 40 kilometers North West of the Eel River mouth shows lower counts of elements used as proxies for terrigenous material. Additionally, all of the profiles are a lot more constant (Figures 25-30).

We can note from this that the recurrence of POC layers increases downcore, for all three cores.

5.2. Sedimentation processes

As we observed, most of the dark POC layers in the cores have a characteristic geochemical signal that exhibits an increase in the Ba/Ti, Fe/Ti, Ca/Si, and S/Fe ratios, as well as a drop in Si/Ti. The increases in Fe/Ti and drop in Si/Ti suggest that the POC layers are composed of organic terrigenous material sourced from the Eel River drainage, as Ti reflects riverine input and Fe/Ti can highlight the presence of pyrite, which is strongly correlated with the presence of organic carbon. Increases in Ba/Ti and Ca/Si would be due to the entraining of organic material from both the shelf and upper slope as the gravity flows course across the Eel Margin (Figure 2). In order to form deposits with such a geochemical signature, indicative of large organic matter, in 400 meters of water, tens of kilometers offshore, gravity flows potentially triggered by flood events are required. The abundance of wood fragments present in the deposits can be explained by damming of the river by earthquake or precipitation induced

landslides (McCullough, 2009). We postulate that the presence of shell fragments in such terrigenous deposits might suggest a larger magnitude flood event, which may have eroded the estuarine deposits and transported inner-shelf shell-rich deposits to the slope. Sr/Ca variability can indicate the relative abundance of terrigenous material versus pelagic calcium carbonate. Lows in Sr/Ca might fingerprint the larger events that might erode nearshore deposits as well as resuspending more pelagic sediments. These events may correlate with damming of the rivers following large earthquakes and hillslope failure, with the sediment liberated during the ensuing wet season and dam collapse.

The two bottom layers, observed in PC01 section 4, having lows in Ba/Ti but large peaks in Fe/Ti and S/Fe, as well as small peaks in Ca/Si and Sr/Ca and a slight decrease in Si/Ti, could be coarse grain, rapidly deposited sand events but with little organic carbon deposition and no resuspension of pelagic material.

Signs of bioturbation, such as in sections 2 of PC02 and PC07, indicate that the sediments present in those core sections stayed longer on the seafloor without rapid subsequent deposition.

The alternating thin POC layers and clay beds in section 4 of PC07 could be the pattern of a warm PDO phase with superimposed El Niño events.

We can highlight that the presence of layers composed of ninety percent of organic carbon, an order of magnitude larger than usual in situ organic carbon levels, at a distance of 27 kilometers from the Eel River mouth appears to be the result from riverine discharge hyperpycnal flows. This shows that they are a process of major importance in the sequestration of organic carbon on the continental slope.

The observed changes in accumulation rates 2600 years BP, at about 800 mm in PC01 and about 3400 mm in PC02, could be explained by a change in the amount of terrigenous material. Almost all the large POC layers visible in PC01 have been deposited prior to that and, similarly, a majority of the POC layers visible in PC02 have also been deposited before.

McCullough (2009) showed that large earthquakes along the Cascadia Margin could make the hillslopes more susceptible to erosion and that, in the last 2000 years, there has been a significant reduction in large earthquakes.

5.3. Climatic variability: The Pacific Decadal Oscillation (PDO)

Climate records from the Pacific provide evidence that coherent modes of variability occur at an interdecadal periodicity. This variability has been termed the Pacific Decadal Oscillation (PDO; Mantua et al. 1997). Sea surface temperatures are below average in the central and western North Pacific Ocean

and above average in the eastern Pacific, during the warm PDO phase. During cool PDO phases, the opposite conditions occur.

The historical record of PDO is relatively short, with records extending back only about a century. Periodicities of 15-25 years and 50-70 years have been found (Minobe, 2000, Tourre et al., 2001, and Chao et al., 2000). Hare (1996) and Minobe (1997) documented that shifts in the PDO have occurred in 1925, 1947, and 1977. During a positive phase of PDO, higher temperatures result in increased evaporation and precipitation. Increases in precipitation may lead to increased erosion on land and increased river discharge. This will also result in the increased probability of hyperpycnal flows.

McCullough (2009) had hypothesized that the fining-upward packages were a signal for phase shifts of the Pacific Decadal Oscillation. Here, we test this hypothesis by using geochemical proxies for input of terrigenous material by river discharge.

Gedalof et al. (2002) combined five previously published proxy records of North Pacific climate variability in order to evaluate the extent to which these records offer a consistent representation of Pacific climate variability. The proxy records of climatic variability used are annual growth increments from trees and coral heads. These records cover a period of time that spans well beyond the first

instrumental records of Pacific climate variability. One question Gedalof et al. (2002) address in their study is whether the PDO is a consistent feature of the North Pacific climate variability or a recent feature, from the twentieth century on. Their study provides a better understanding of the long-term behavior of the PDO. The PDO seems to have been present since at least 1600, but varied in magnitude through time. Gedalof et al. (2002) used a principal components analysis to compare the chronologies and determine modes of variance common to the five chronologies, providing an estimate of the strength of the common signal between the chronologies. The analysis they present is restricted to the interval common to all of the proxy records, which is between 1840 and 1990. The correlation between the results of Gedalof et al. (2002) study and the PDO index is greater than for any of the individual proxy records with the PDO index. As such, this would indicate that the combined chronologies capture the variability better than the individual studies. Together, these results suggest that the PDO has not been coherent through time; it has been operative since at least 1600, but of little influence over most of the nineteenth century. Three dominant waveforms have been observed in their analysis, with periods of 85, 23, and 20 years (though it is still unclear whether the 20 and 23 year modes are actually distinct or artifacts). Together, these three waveforms explain over 50 percent of the variance in PDO index, while capturing the observed phase shifts in the twentieth century.

MacDonald and Case (2005) produced a tree ring chronology from *Pinus flexilis* in both California and Alberta, reconstructing the PDO strength and variability over a period of 993 to 1996 AC. The reconstruction indicates periodicities of the PDO to be 50 to 70 years for the last 200 years, and 50 to 100 years between 1500 and 1300 and 1200 to 1000. In order to have a representative reconstruction of the PDO, MacDonald and Case sampled trees at the two ends of the precipitation dipole of the PDO, at Mount San Gorgonio in southern California and at Whirlpool Point in Alberta. The most important feature of the reconstruction is a strong negative PDO phase between 993 and 1300 AD, which corresponds to a severe period of drought in western and central North America. Additionally, for the same period, there is evidence for cooler northeast Pacific sea surface temperatures, higher rates of upwelling, and increased coastal marine productivity. The wavelet spectrum resulting from MacDonald and Case's study suggests that a 50-year period is a significant mode of variability over the past millennium. However, this 50-year mode of variability is not consistently present over that time interval and reveals a significant weakening between 1200 and 1300 and 1500 and 1800. The typical PDO variability over the past two hundred years has not been a stable feature of the PDO. The 50 to 70 year PDO mode of variability weakened or disappeared for periods in the 19th, 17th, and 13th centuries.

Through these studies, it is clear that the PDO mode of variability has changed over the past millennium, could have changed prior to that, and can be expected to change in the future as well.

Though the geochemical data of our cores does not allow resolving the time scale covered by the previously mentioned studies, this could be a unique climate reconstruction for the last five millennia. The Fe/Ti data is plotted for the whole cores of PC01 and PC02 because it is a proxy for riverine input of terrigenous organic material and peaks in Fe/Ti in the sediments record flood events. Positive PDO phases may be marked by larger flood events. PC07 does not have dating and consequently no time intervals can be calculated.

Looking at Figure 31, we see that only one POC layer is visible in the top 1300 mm of the PC01 core. Based on the radiocarbon dates from Figure 9, this shows that only one POC layer was deposited in the last 3130 years BP. Another large interval with only two small POC layers is observed between 2600 and 3850 mm from the top of the core, or about 3583 and 4175 years BP. During this time span of approximately 600 years, only two events occurred, while 5 occurred in the previous 500 years and 6 occurred in the following 450 years. The dominant recurrence intervals between the POC layers in the time intervals between 3583 BP and 3130 BP and 4758 and 4175 BP are about 30, 50, and about a hundred years. More research is required to determine if these periods of

more and less flood deposits on the margin record modes in the magnitude of PDO. Earthquakes in the region cause either hill slope failure and damming of the valleys or makes the hill slopes more susceptible to erosion. Increased rainfall associated with stronger PDO could explain the observed variation of flood deposits on the slope through time (Figure 31).

For PC02 (Figure 32), two POC layers are deposited after 2000 years BP, at about 580 and 2000 millimeters of depth. 835 years separate these two events. Downcore, the next POC layer is observed at a depth of 4460 millimeters down core, which is approximately 2912 BP. Four POC layers were deposited before that, the first one recorded in this core being at a depth of 7000 millimeters, or 3570 years BP. Besides from the three POC layers that are also recorded in core PC01, centered at about 3300 years BP, which have separation intervals of about 50 and 25 years, the time intervals separating the POC layers in PC02 are of the order of several hundred years.

Considering the intervals between the POC layers, the present study shows that common recurrence patterns are between 20 to 30 years and 40 to 50 years, or hundreds of years, mainly 120 to 150 years (Figures 31 and 32). After 2900 BP, very few POC layers have been deposited: two in PC02 and one in PC01. It appears that more POC layers were deposited prior to 2900 years BP, with POC

layers being more abundant in the bottom of the sediment cores and much more abundant in PC01 than in both PC02 and PC07.

PC01, being on the downslope or erosional portion of the antidune, has a more condensed section (Figure 2). As such, the age of the sediment increases and decreases at a greater rate away from the coarse-grained layer used to correlate the cores than the age of the sediment in PC02 (Figure 9). The accumulation rate for PC07 is predicted to be even higher than in PC02 and thus record less time. Accordingly, the oldest dated material in PC01 is 4758 years BP and the oldest material dated in PC02 is 3727 years BP (Figure 9). Consequently, PC02 (Figure 32) and PC07 (Figure 33) failed to sample any of the POC layers acquired in PC01 below 3000 mm, which is approximately 3839 years BP.

While climate alone cannot explain the deposition of layers so rich in terrigenous organic carbon through hyperpycnal flows, their recurrence interval could be linked to climatic patterns, such as the PDO, that cause floods and flushes the drainage system. Major depositional events could also be linked to earthquake-induced landslides. One might postulate that more large earthquakes occurred in the past, prior to 2000 years BP, along the Cascadia subduction zone and this may explain the occurrence of POC layers offshore, on the slope of the Eel Margin. Clearly more research is required to address this question and provide a better chronology for PC07 and PC05.

5.4. Geochemical Core correlation

Cores PC01 and PC02 have been correlated using the geochemistry data. The largest peak in Fe/Ti ratio, located at a depth of 1540 to 1630 mm in PC01 and 5680 mm to 5900 mm in PC02, has been used for the correlation. This peak in Fe/Ti ratio corresponds to a large terrigenous event. The geochemical signature of these layers in both cores is typified by increases in Ba/Ti, Fe/Ti, Ca/Si, Sr/Ca, and S/Fe. This event also corresponds to the largest peak in grain size, which was used to do a previous correlation between the cores (McCullough, 2009). Two other organic layers can be correlated across the two cores, one above the peak event and one below. The time intervals, calculated from the accumulation rates, between those three events are similar in core PC01 and PC02: about 50 years between the first and the second layer and 25 years between the second and the third one. The correlation between PC01 and PC02 is consistent with the correlation based on radiocarbon dating. In order to correlate PC07 with cores PC01 and PC02, the largest peak in Fe/Ti was also used. This peak in Fe/Ti is located at a depth of 4300 to 4500 mm. This, however, does not correspond with the largest peak in grain size but is the second largest peak in grain size data (Figure 9). Additionally, a POC layer below this main event is observed in PC07, at about 4600 mm, but no POC layer is visible above it, as in PC01 and PC02.

Other element ratios have been used to make a similar correlation. The largest peaks in Sr/Ca (Figure 35) and S/Fe (Figure 36) ratios data are also observed at the same depths. Some artifacts are present in the S/Fe ratio plots. The abnormally high values are due to cracks in the core sediment.

This correlation has been made based solely on the geochemistry of the cores. Dating on core PC07 would be needed to make a definite correlation between all three cores. The setting of the cores in an anti-dune, which is a major constraint, does not necessarily support the geochemical correlation of the cores. However, with the cores correlated based on the grain size, POC layers depths in PC07 do not correspond with cores PC01 and PC02.

6. Conclusion

This geochemical analysis of four cores from the Eel River margin points to the importance of hyperpycnal flows in the sequestration of organic carbon in the ocean. Hyperpycnal flows, transporting terrigenous POC across the continental margin and to the top of the slope, result in very rapid deposition of layers several centimeters thick of terrigenous material, including a large fraction of organic carbon. Short-term sediment processes associated with flood-events are a dominant control on long-term sedimentation and on the sequestration of terrigenous organic carbon on the Eel margin. Carbon burial and sedimentation on the Eel margin may be largely controlled by precipitation events and annual and decadal climate variability. Changes in sedimentation rates in the cores seem to be mainly due to changes in terrestrial input by the river. The geochemical signature of the terrigenous POC deposits can help us understand the magnitude of the flood events.

A core correlation between PC01, PC02, and PC07 has been proposed based on the geochemical analysis. Additional dating on the cores could provide better constraints on the core correlation that was made using the XRF data.

Appendices: Figures 1-36 and Tables 1-5.

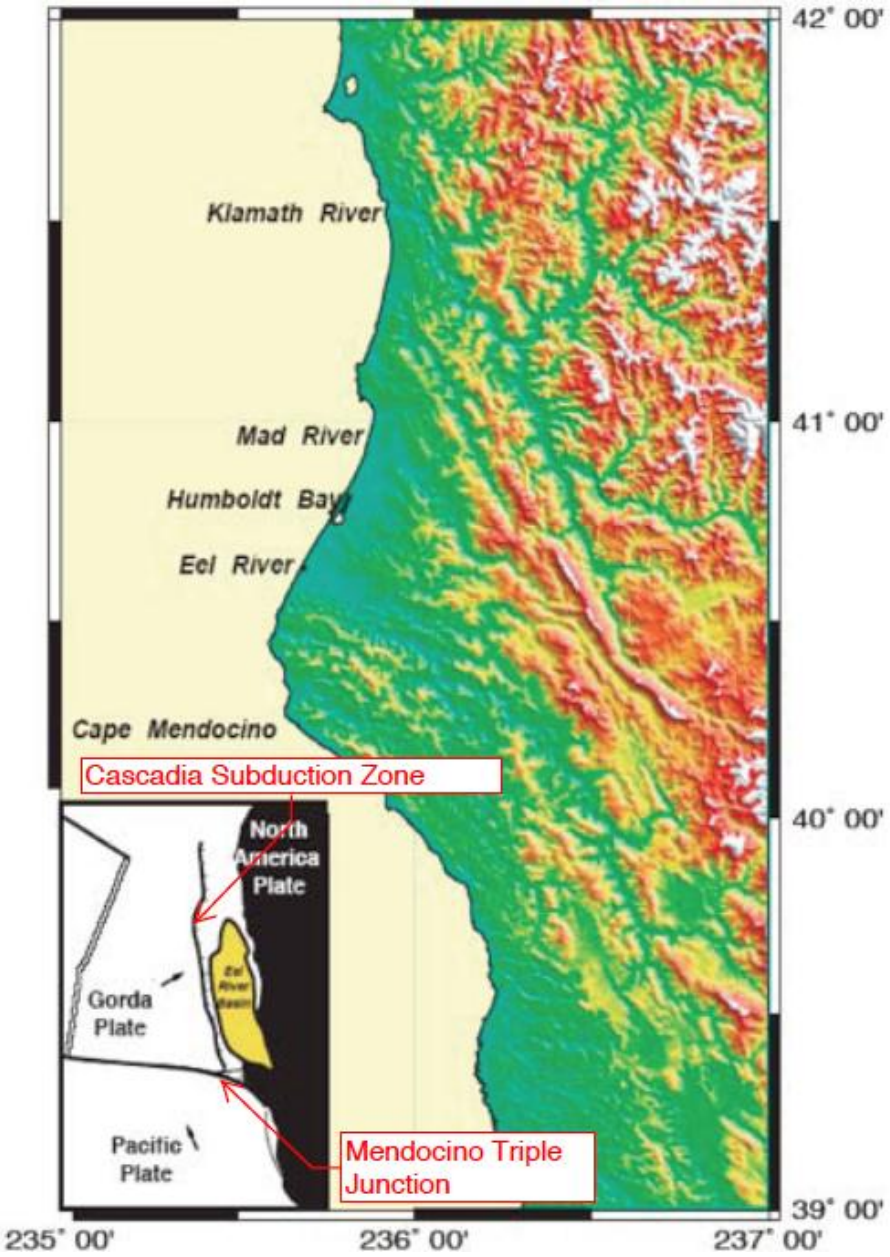

Figure 1. Geological setting of the Eel River margin, north of the Mendocino Triple Junction. Image courtesy of Driscoll (2010).

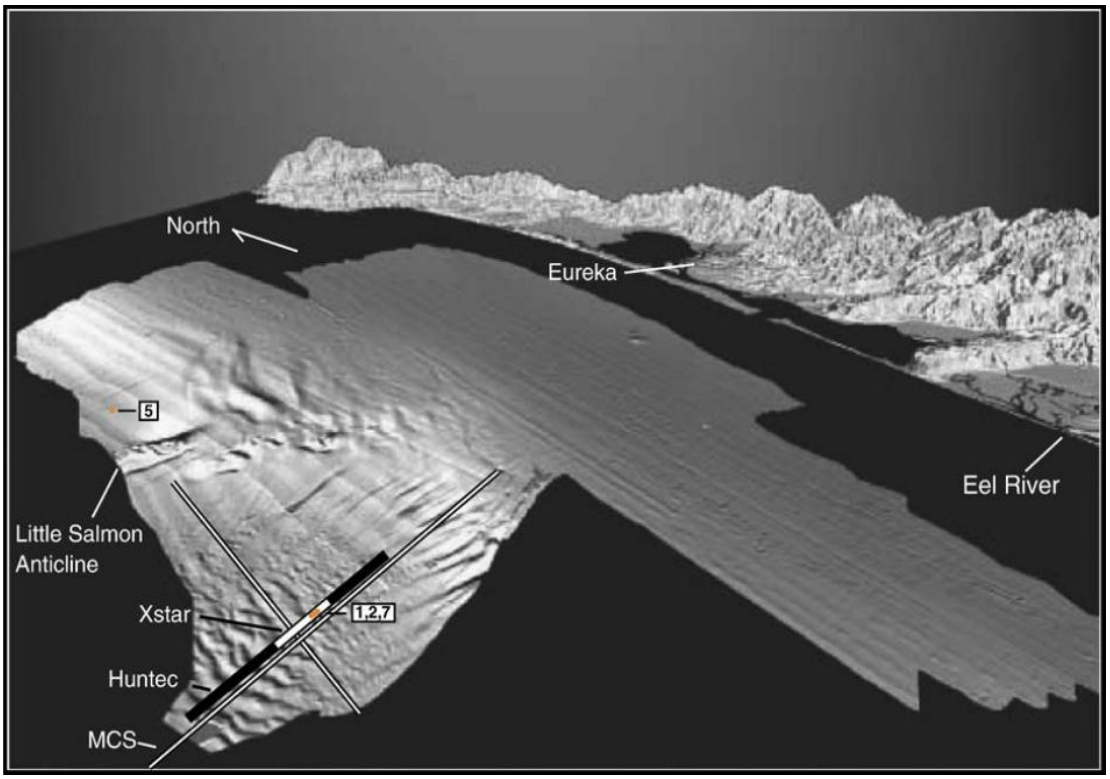

Figure 2. Location of the four cores (in red) and the CHIRP, Huntec, and multi-channel seismic lines on a bathymetry map of the Humboldt Slide. Image from Schwehr et al. (2007).

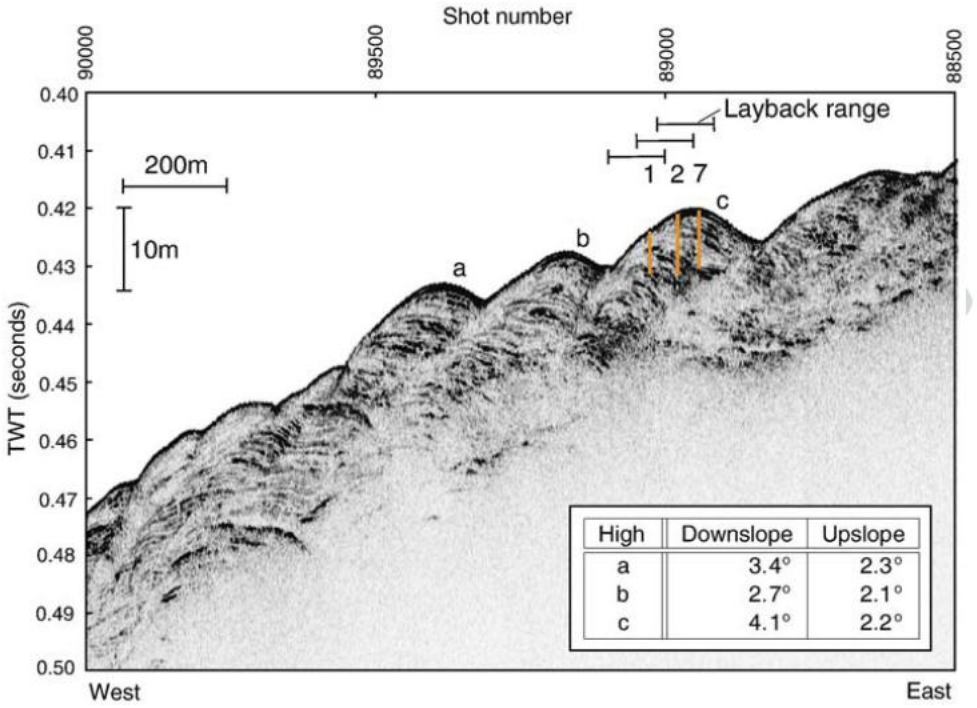

Figure 3. CHIRP seismic line showing the location of the cores on the Humboldt Slide. Image from Schwehr et al. (2007)

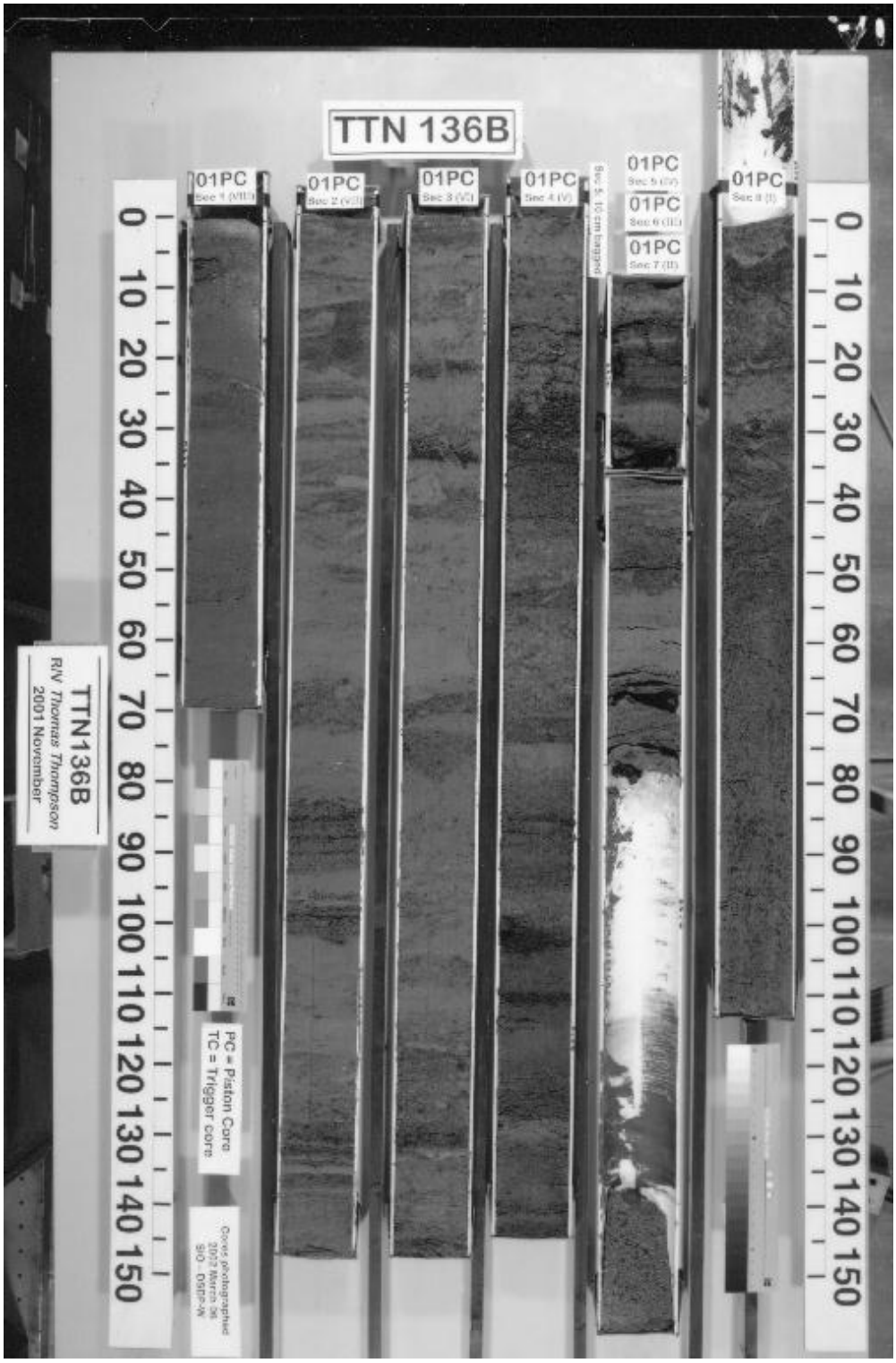

Figure 4. Piston Core 01 sections. Only sections 1 to 4 were used for the purpose of this study. Dark layers are visible in the sediments of sections 2, 3, and 4. Photo from McCullough.

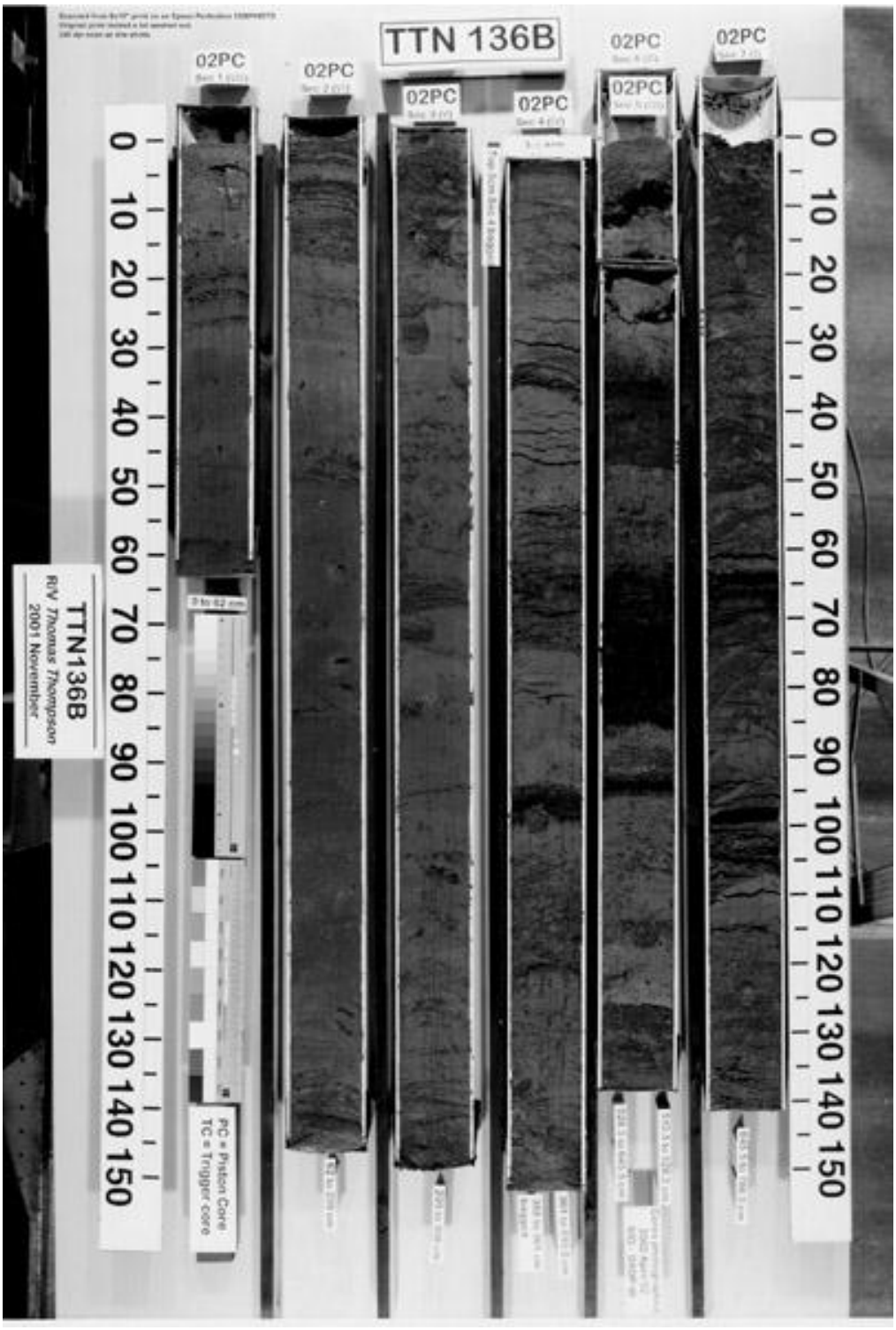

Figure 5. Piston Core 02 sections. Dark layers are visible in the sediments, particularly in sections 4 and 6. Photo from McCullough.

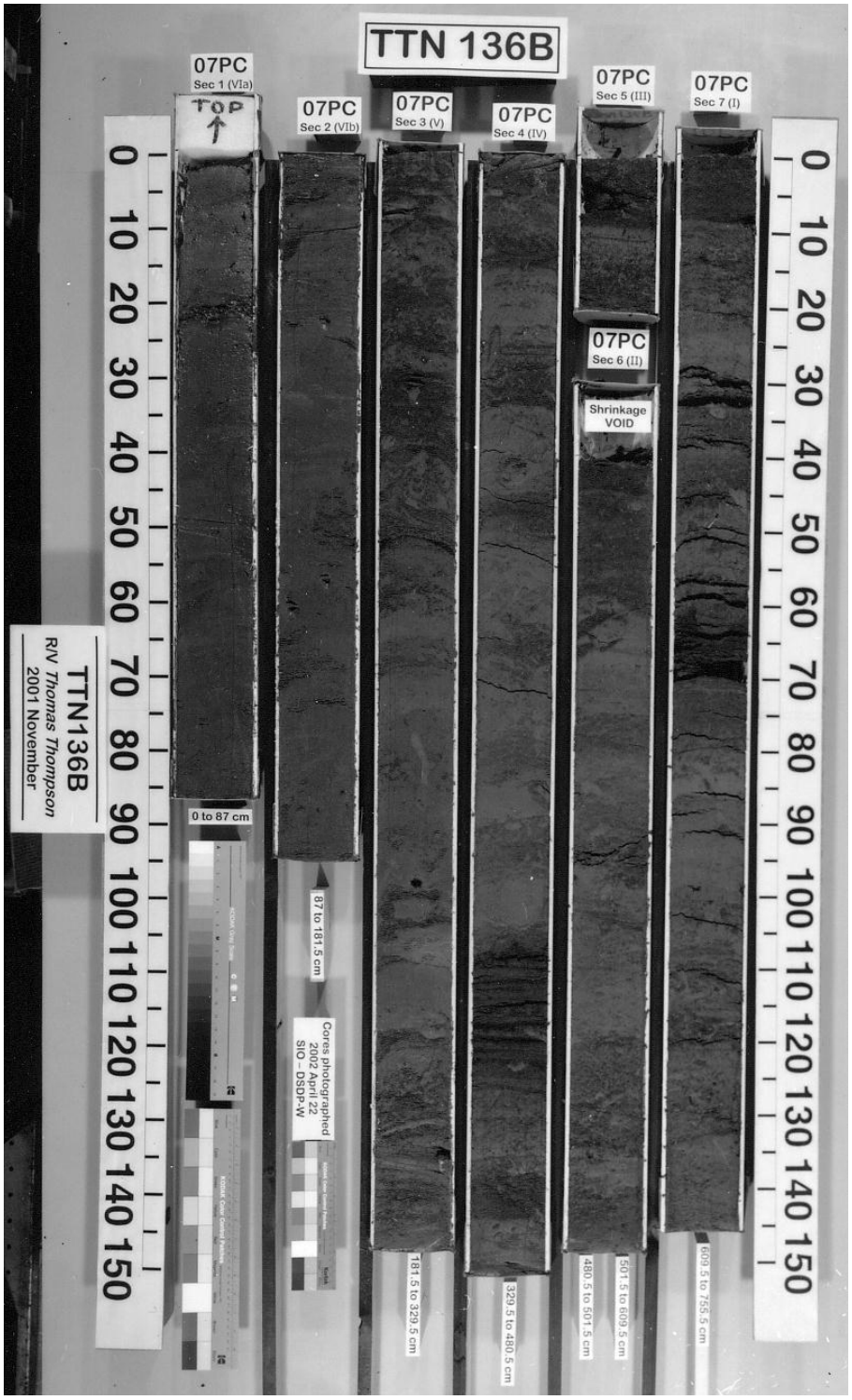

Figure 6. Piston Core 07 sections. A number of dark layers are visible in this core, particularly in the deeper sections of the core. Photo from McCullough.

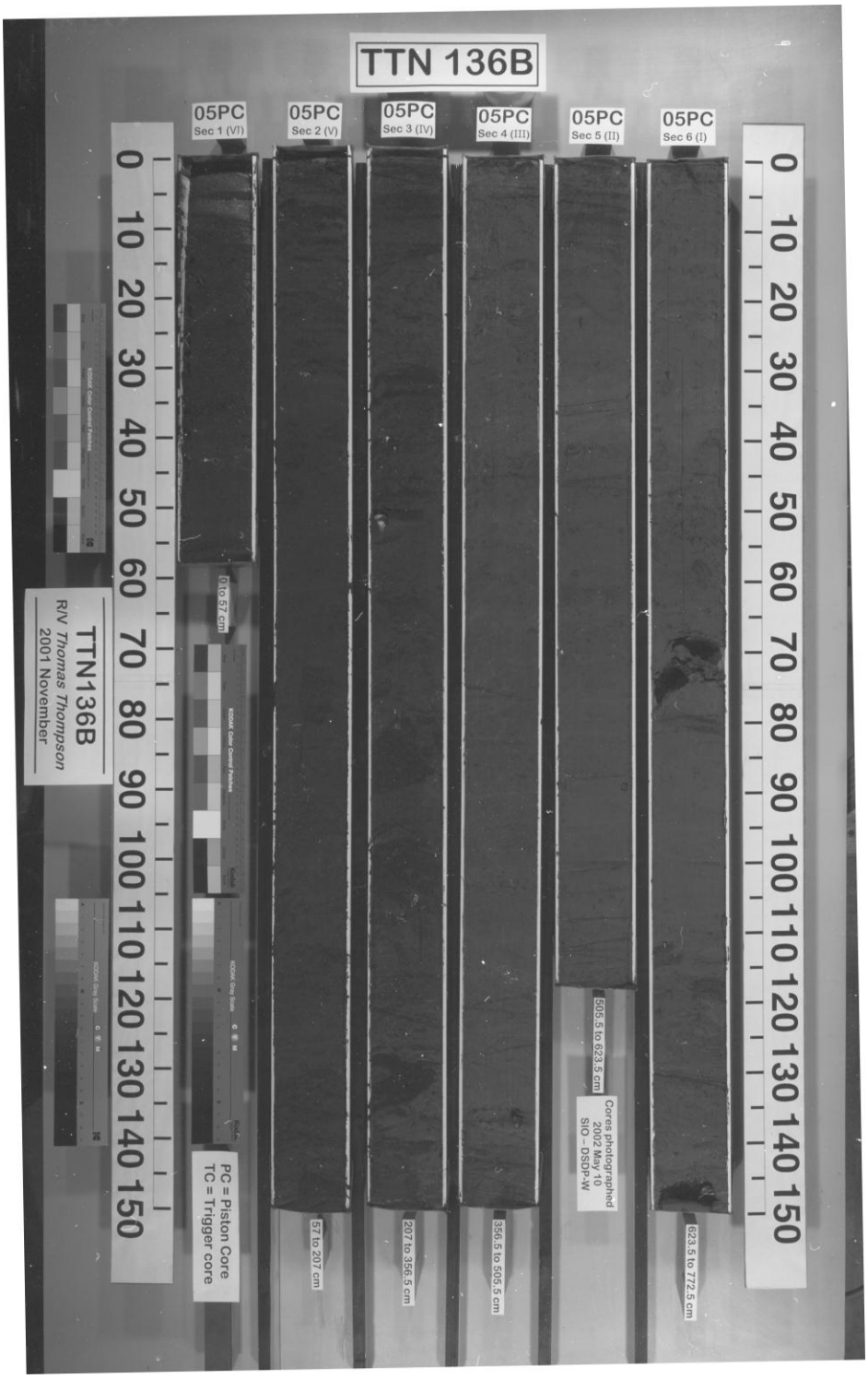

Figure 7. Piston Core 05 sections. No dark layers are visible in this core. Photo from McCullough.

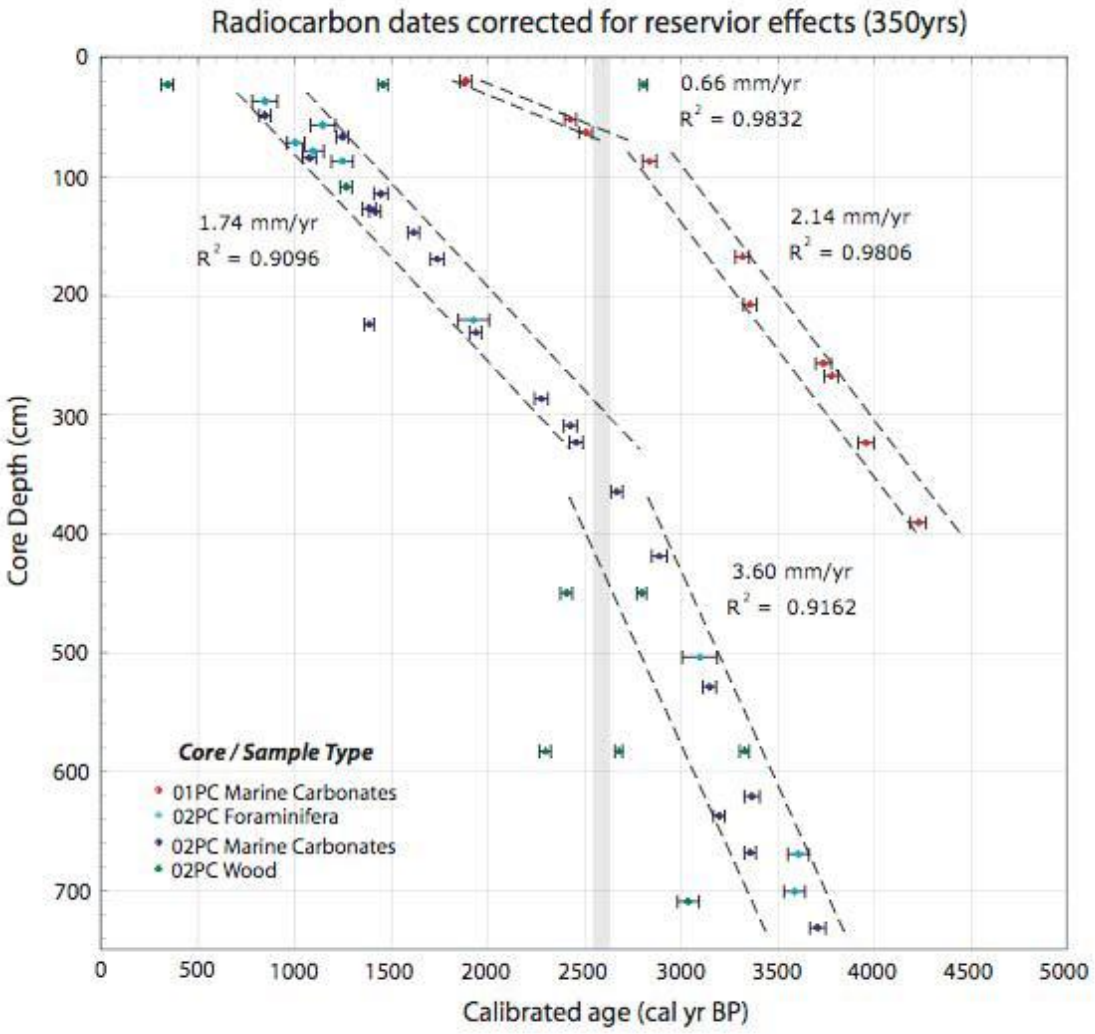

Figure 8. Accumulation rates for cores PC01 and PC02 based on linear regressions of radiocarbon ages of marine carbonate tests. Accumulation rate for core PC01 is less than that of core PC02. Both cores exhibit a change in accumulation rate at about 2600yr BP. Figure courtesy of McCullough (2008).

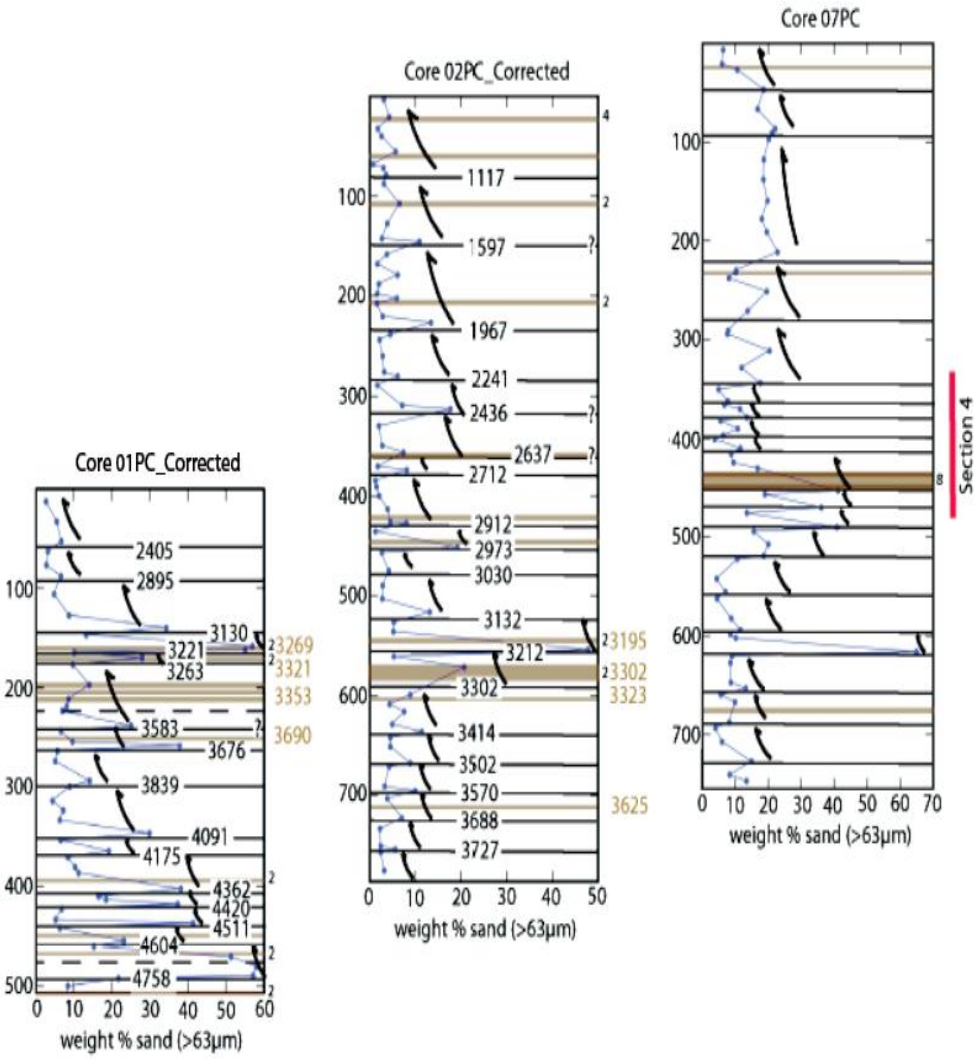

Figure 9. Core correlation. Brown lines represent POC layers. Dates (yrs BP) corresponding to the POC layers, colored brown, were calculated linearly using the closest radiocarbon date above and below the base of the layer. Black lines represent bases of the fining-upward packages. Question marks denote fining-upward packages that were not identified visually when examining the core and were reinterpreted to be bases based on the grain size distribution. Dashed lines represent those bases that were initially identified visually, but were reinterpreted and disregarded based on the grain size distribution (McCullough, 2009).

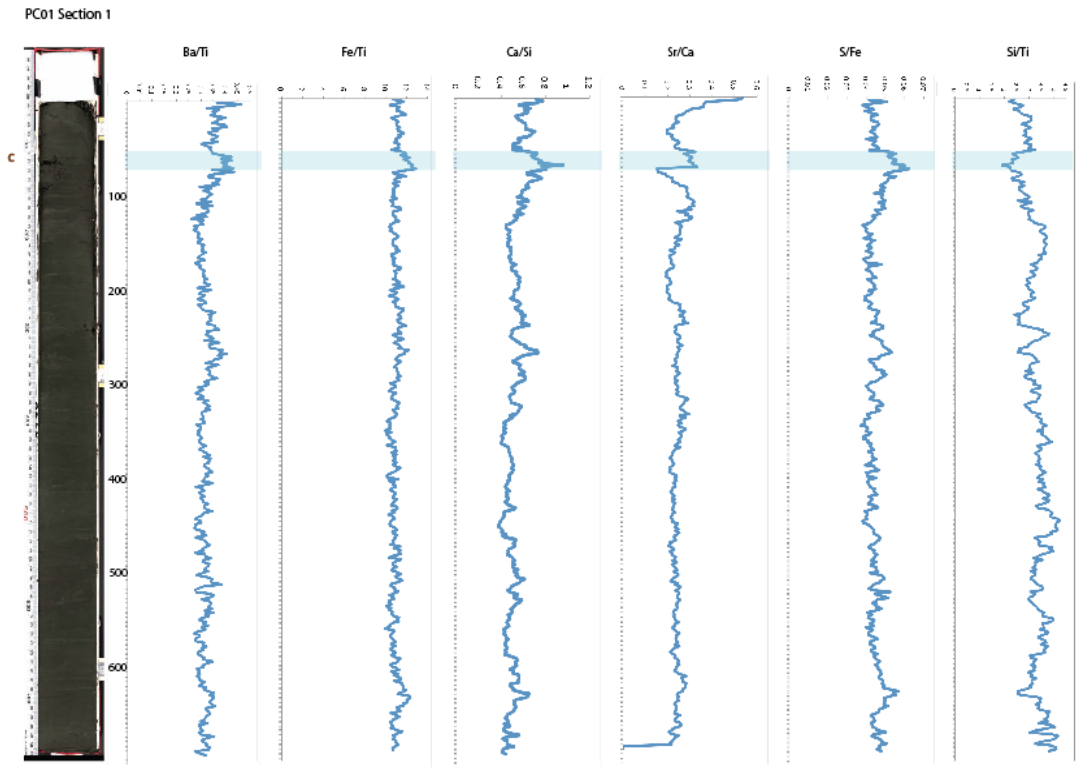

Figure 10. Core image and Ba/Ti, Fe/Ti, Ca/Si, Sr/Ca, S/Fe, and Si/Ti ratio plots for PC01 Section 1. Horizontal axes are the ratio values and vertical axes are depth down the core section in millimeters. Dark layers in the sediments are highlighted in blue in the ratio plots. Cracks in the cores are pointed out by the letter "c", in brown.

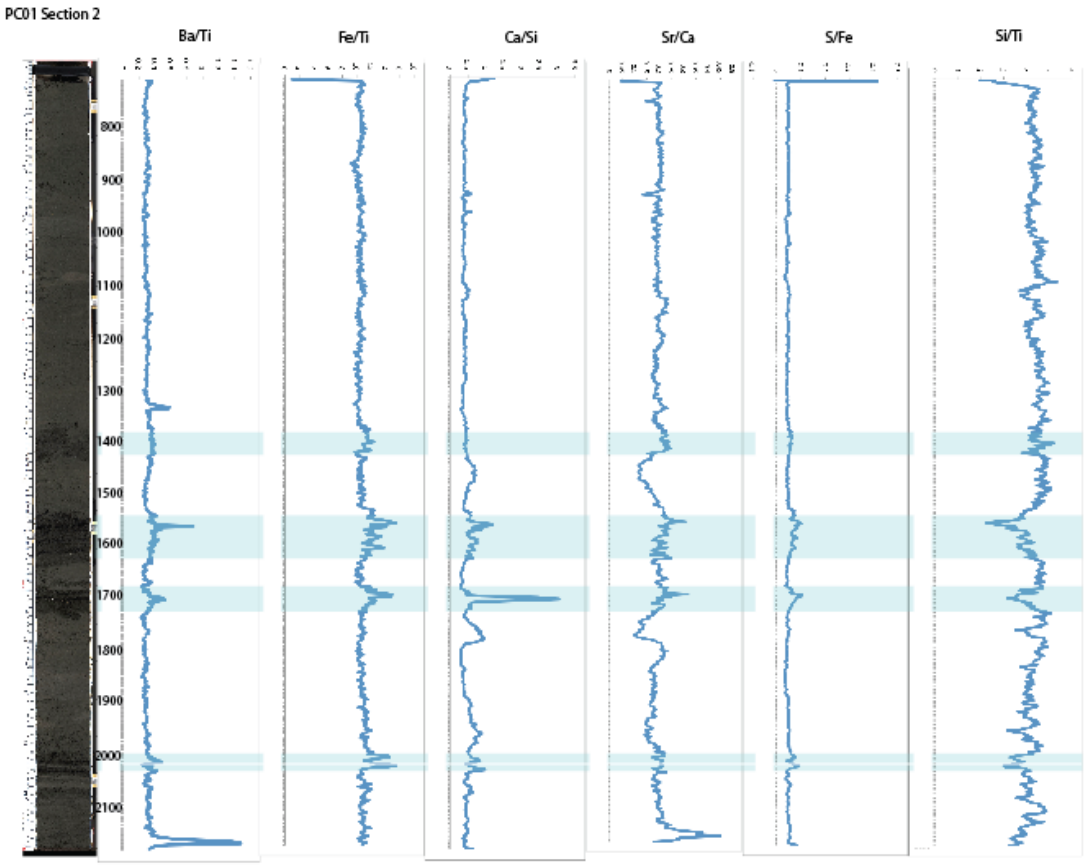

Figure 11. Core image and Ba/Ti, Fe/Ti, Ca/Si, Sr/Ca, S/Fe, and Si/Ti ratio plots for PC01 Section 2. Horizontal axes are the ratio values and vertical axes are depth down the core section in millimeters. Dark layers in the sediments are highlighted in blue in the ratio plots.

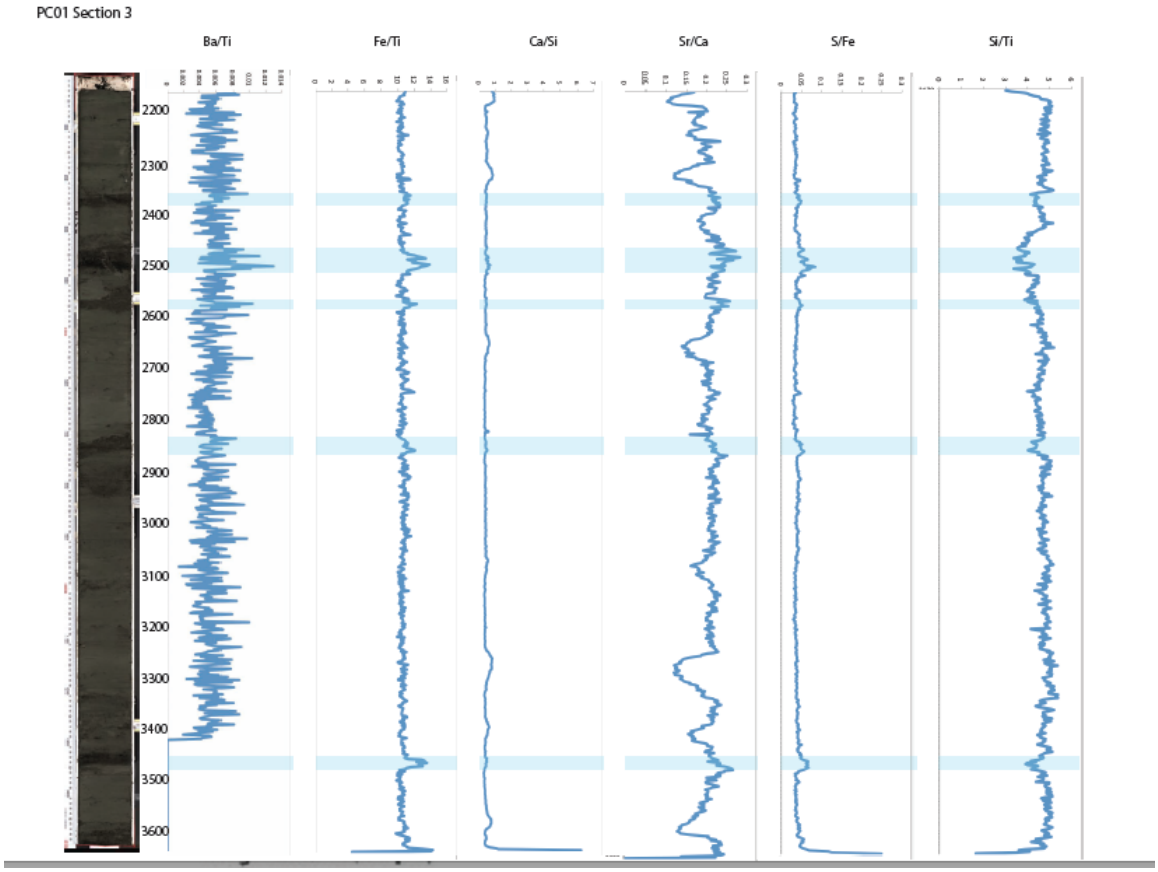

Figure 12. Core image and Ba/Ti, Fe/Ti, Ca/Si, Sr/Ca, S/Fe, and Si/Ti ratio plots for PC01 Section 3. Horizontal axes are the ratio values and vertical axes are depth down the core section in millimeters. Dark layers in the sediments are highlighted in blue in the ratio plots.

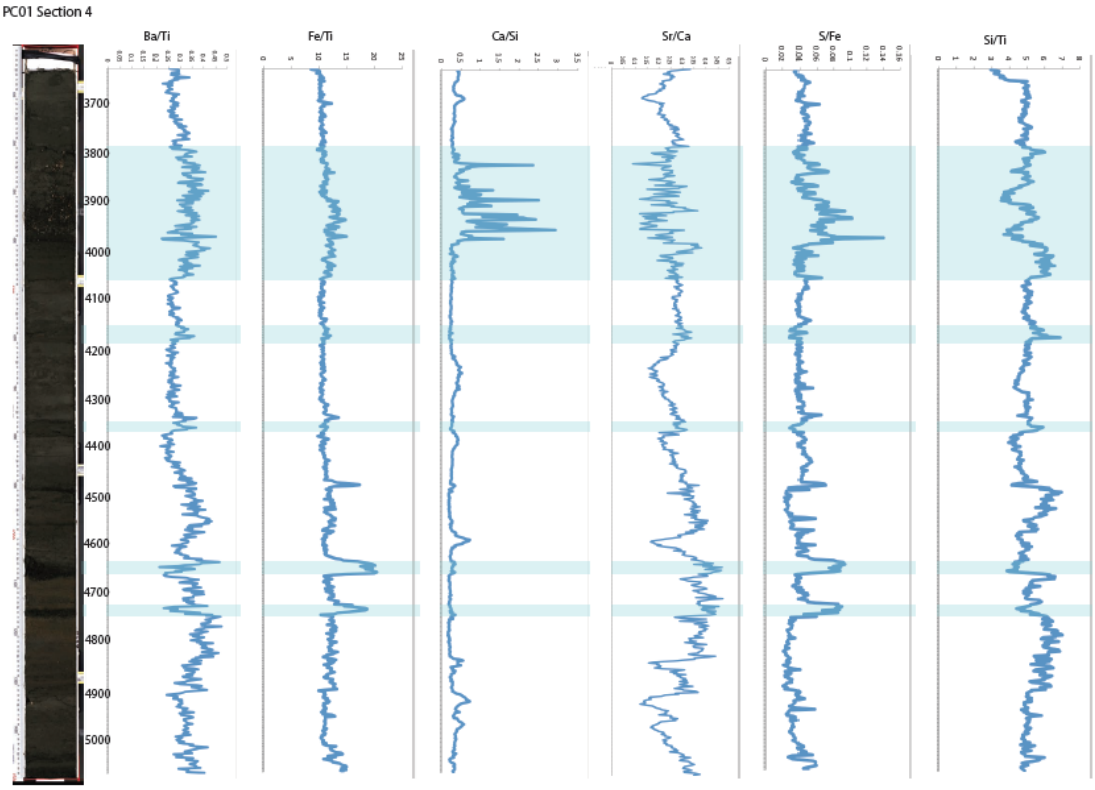

Figure 13a. Core image and Ba/Ti, Fe/Ti, Ca/Si, Sr/Ca, S/Fe, and Si/Ti ratio plots for PC01 Section 4. Horizontal axes are the ratio values and vertical axes are depth down the core section in millimeters. Dark layers in the sediments are highlighted in blue in the ratio plots.

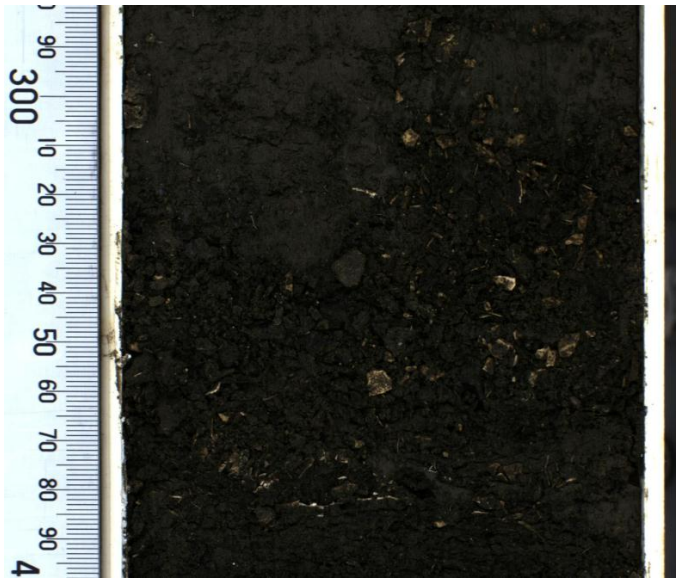

Figure 13b. Shell fragments are visible in the first terrigenous POC layer of this core section, from about 3800 to 4000 mm from the top of the core.

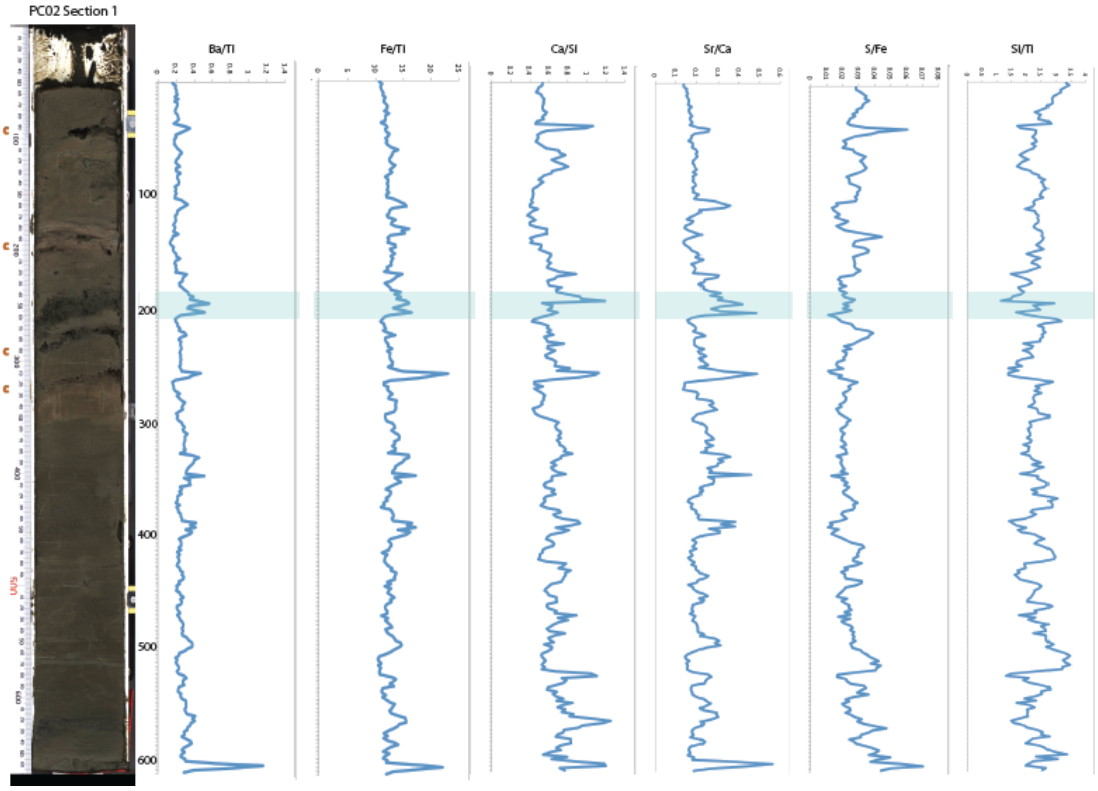

Figure 14. Core image and Ba/Ti, Fe/Ti, Ca/Si, Sr/Ca, S/Fe, and Si/Ti ratio plots for PC02 Section 1. Horizontal axes are the ratio values and vertical axes are depth down the core section in millimeters. Dark layers in the sediments are highlighted in blue in the ratio plots. The letter "c", in brown, points out cracks in the cores.

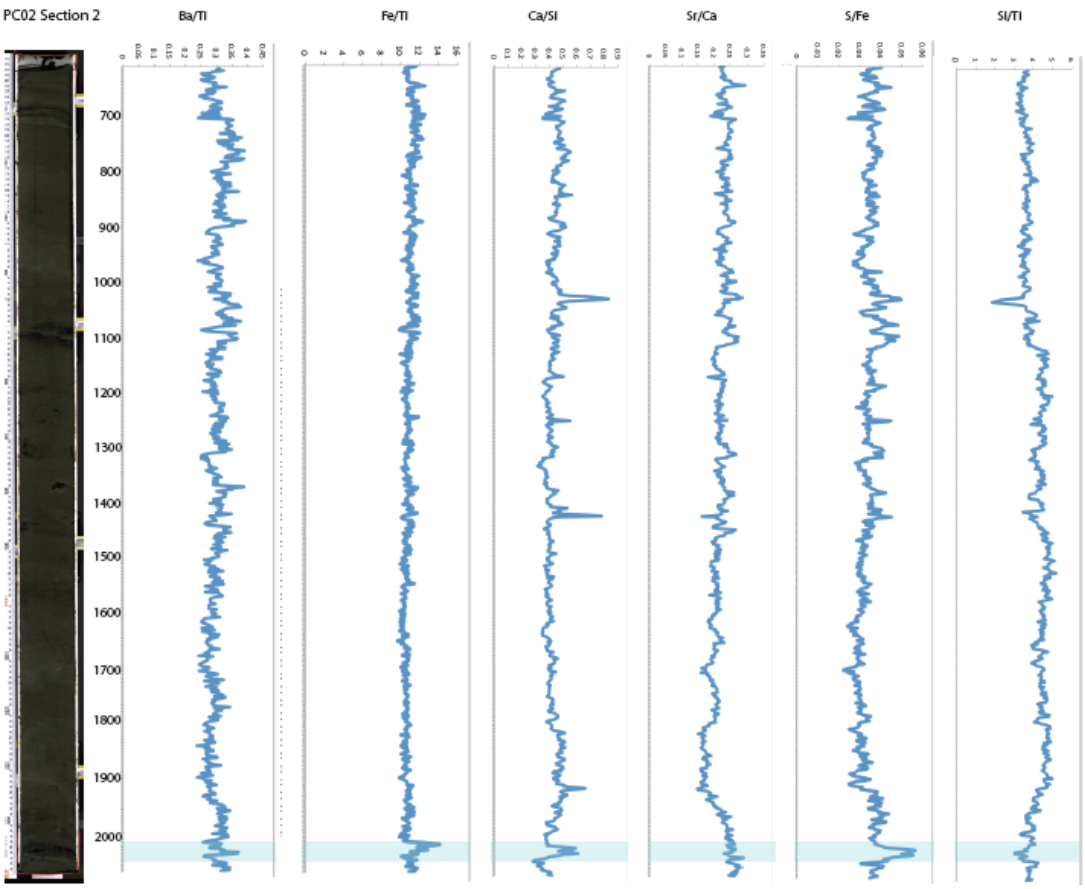

Figure 15. Core image and Ba/Ti, Fe/Ti, Ca/Si, Sr/Ca, S/Fe, and Si/Ti ratio plots for PC02 Section 2. Horizontal axes are the ratio values and vertical axes are depth down the core section in millimeters. Dark layers in the sediments are highlighted in blue in the ratio plots.

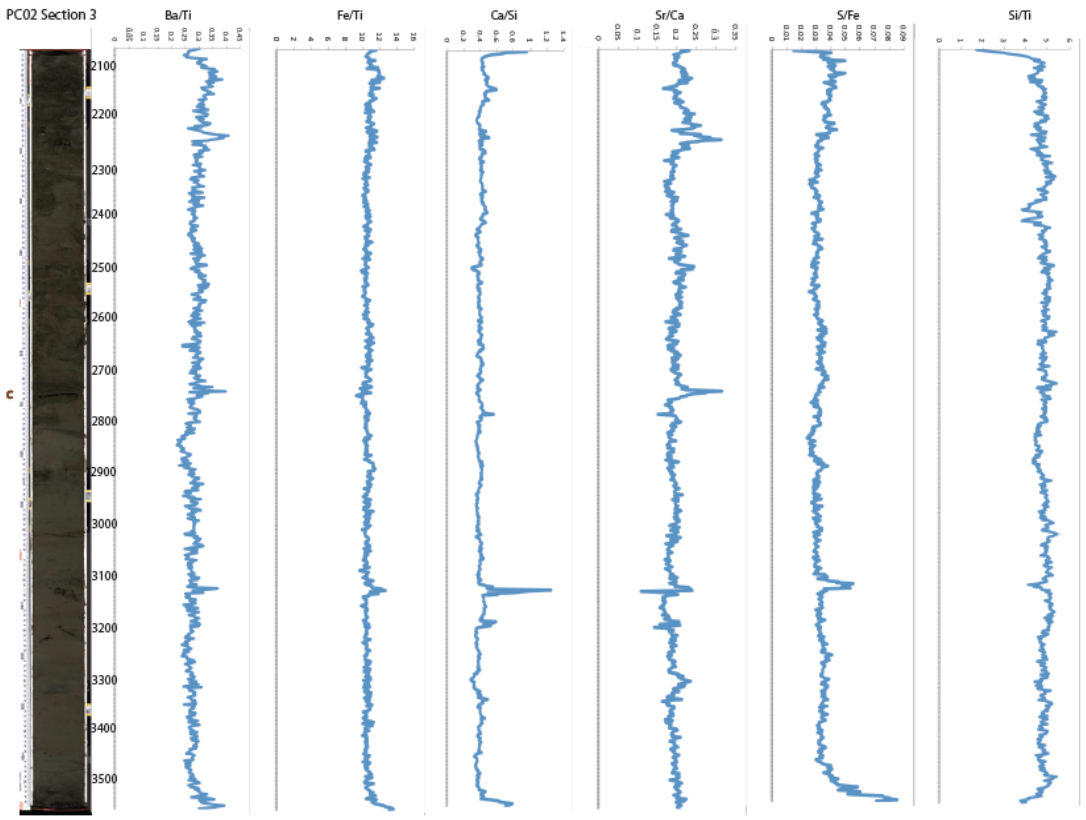

Figure 16. Core image and Ba/Ti, Fe/Ti, Ca/Si, Sr/Ca, S/Fe, and Si/Ti ratio plots for PC02 Section 3. Horizontal axes are the ratio values and vertical axes are depth down the core section in millimeters. Brown letters "c" show cracks in the sediments.

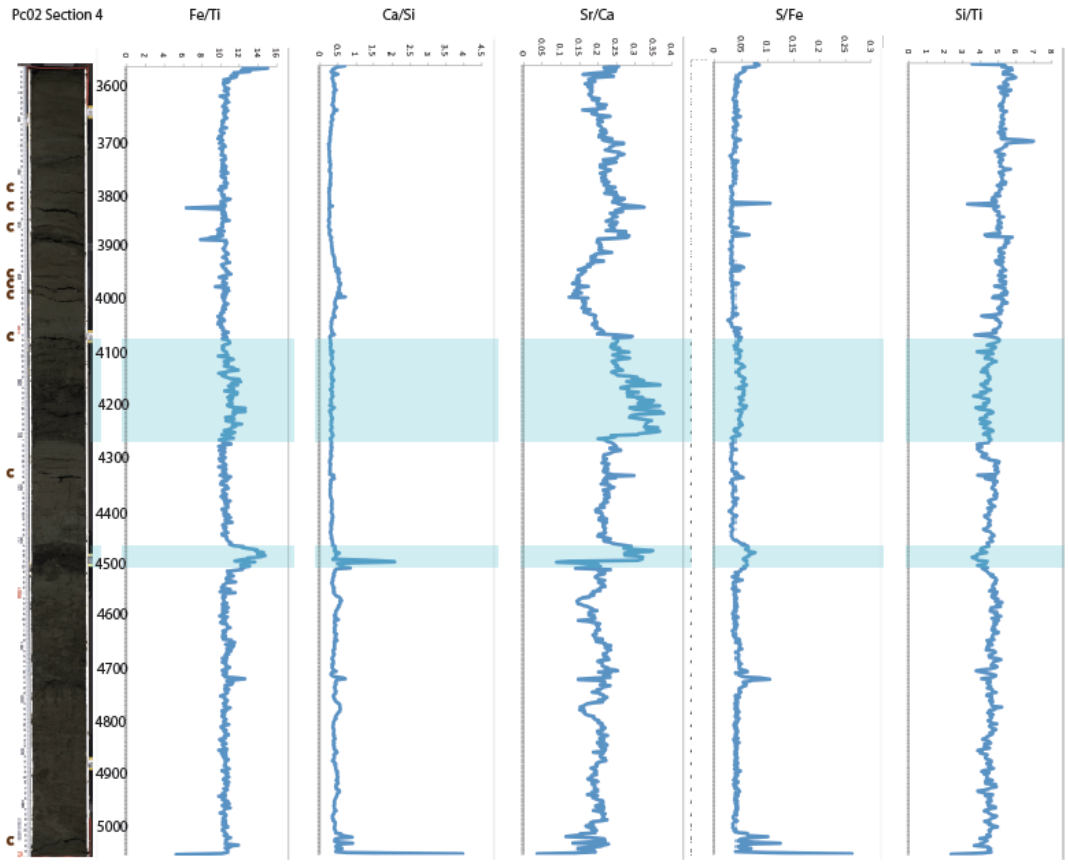

Figure 17. Core image and Ba/Ti, Fe/Ti, Ca/Si, Sr/Ca, S/Fe, and Si/Ti ratio plots for PC02 Section 4. Horizontal axes are the ratio values and vertical axes are depth down the core section in millimeters. Dark layers in the sediments are highlighted in blue in the ratio plots. Brown letters "c" show cracks in the sediments.

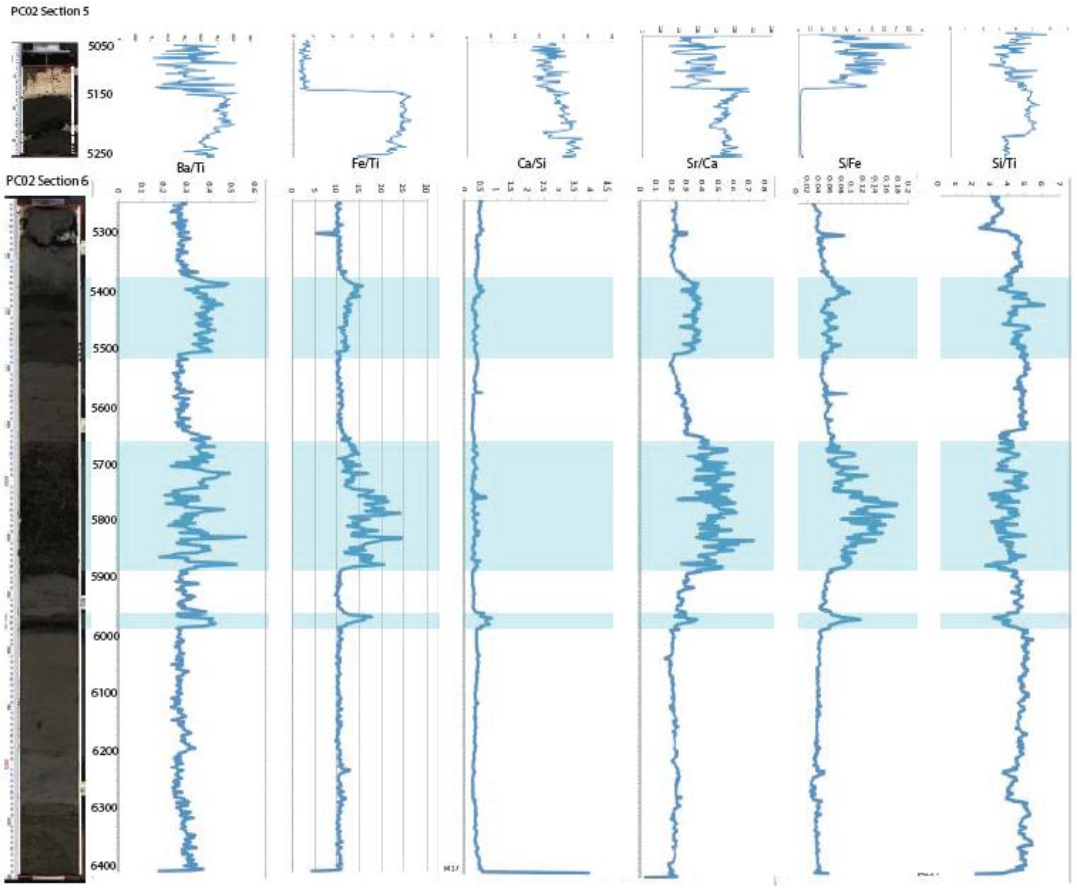

Figure 18a. Core image and Ba/Ti, Fe/Ti, Ca/Si, Sr/Ca, S/Fe, and Si/Ti ratio plots for PC02 Sections 5 and 6. Horizontal axes are the ratio values and vertical axes are depth down the core section in millimeters. Dark layers in the sediments are highlighted in blue in the ratio plots.

Figure 18b. Wood fragments are visible in the sediment between 5650 mm and 5800 mm.

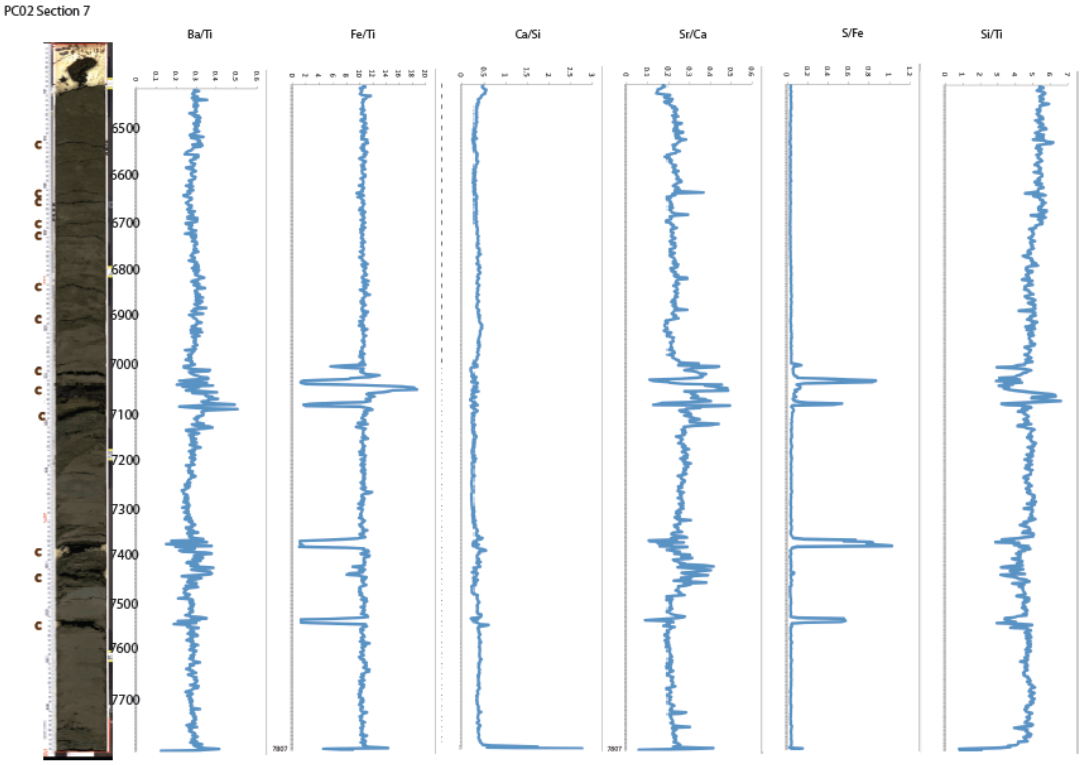

Figure 19. Core image and Ba/Ti, Fe/Ti, Ca/Si, Sr/Ca, S/Fe, and Si/Ti ratio plots for PC02 Section 7. Horizontal axes are the ratio values and vertical axes are depth down the core section in millimeters. Brown letters "c" show cracks in the sediments.

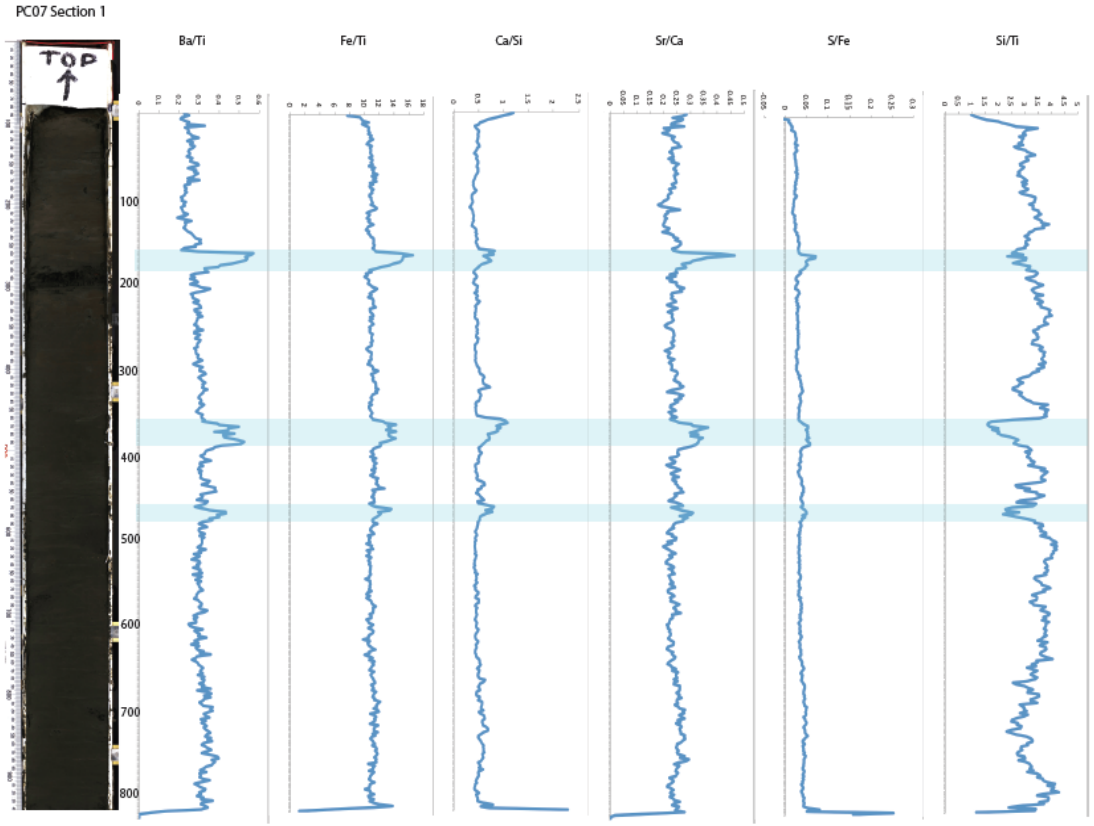

Figure 20. Core image and Ba/Ti, Fe/Ti, Ca/Si, Sr/Ca, S/Fe, and Si/Ti ratio plots for PC07 Section 1. Horizontal axes are the ratio values and vertical axes are depth down the core section in millimeters. Dark layers in the sediments are highlighted in blue in the ratio plots.

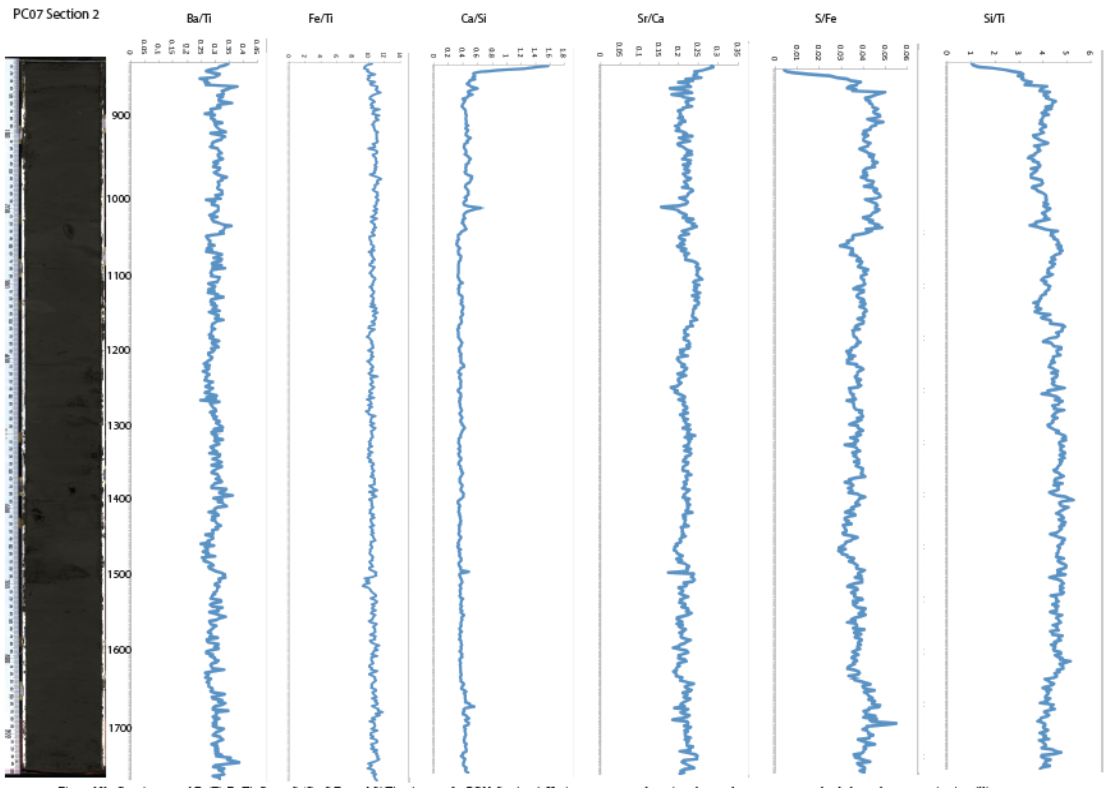

Figure 21. Core image and Ba/Ti, Fe/Ti, Ca/Si, Sr/Ca, S/Fe, and Si/Ti ratio plots for PC07 Section 2. Horizontal axes are the ratio values and vertical axes are depth down the core section in millimeters.

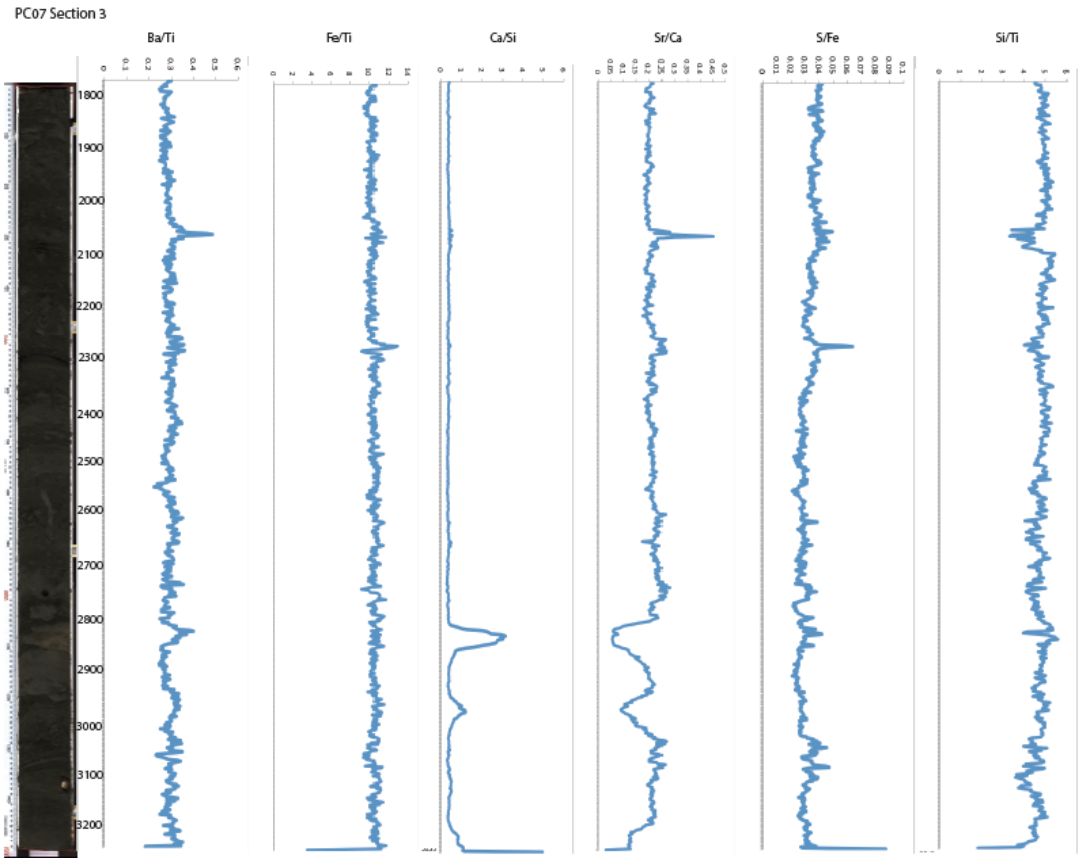

Figure 22a. Core image and Ba/Ti, Fe/Ti, Ca/Si, Sr/Ca, S/Fe, and Si/Ti ratio plots for PC07 Section 3. Horizontal axes are the ratio values and vertical axes are depth down the core section in millimeters.

Figure 22b. Large shell present at 3100 mm from the top of the core.

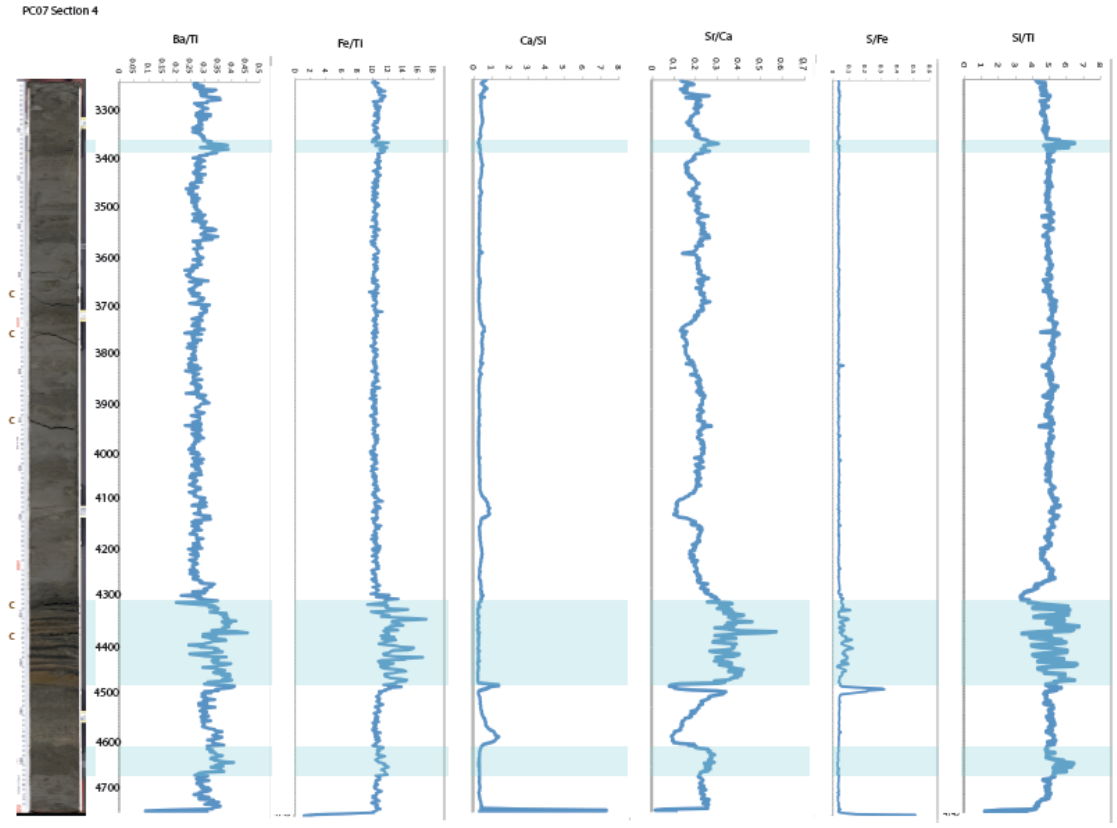

Figure 23a. Core image and Ba/Ti, Fe/Ti, Ca/Si, Sr/Ca, S/Fe, and Si/Ti ratio plots for PC07 Section 4. Horizontal axes are the ratio values and vertical axes are depth down the core section in millimeters. Dark layers in the sediments are highlighted in blue in the ratio plots. Brown letters "c" show cracks in the sediments.

Figure 23b. Alternating thin POC layers and clay beds, between 4301 and 4500 mm from the top of the core.

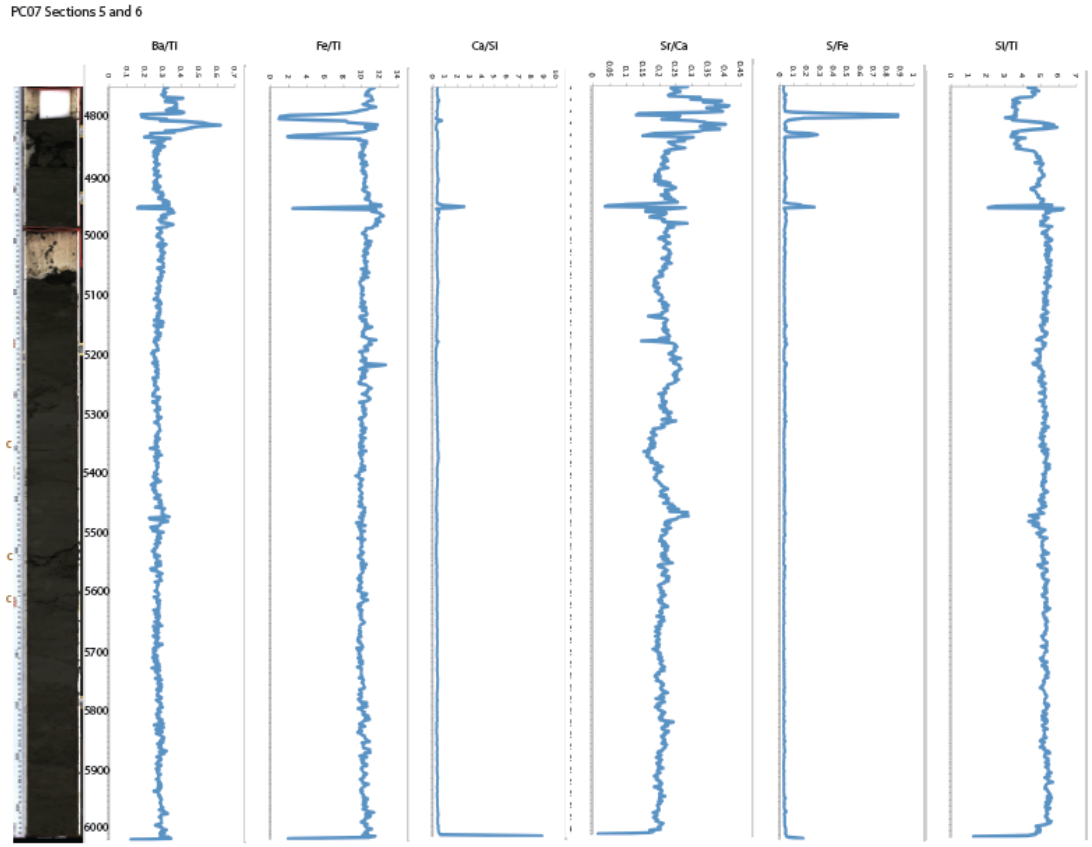

Figure 24. Core image and Ba/Ti, Fe/Ti, Ca/Si, Sr/Ca, S/Fe, and Si/Ti ratio plots for PC07 Sections 5 (top, from 4800 to 5000 mm) and 6 (bottom, from 5100 to 6000 mm). Horizontal axes are the ratio values and vertical axes are depth down the core section in millimeters. The letter "c", in brown, points out cracks in the cores.

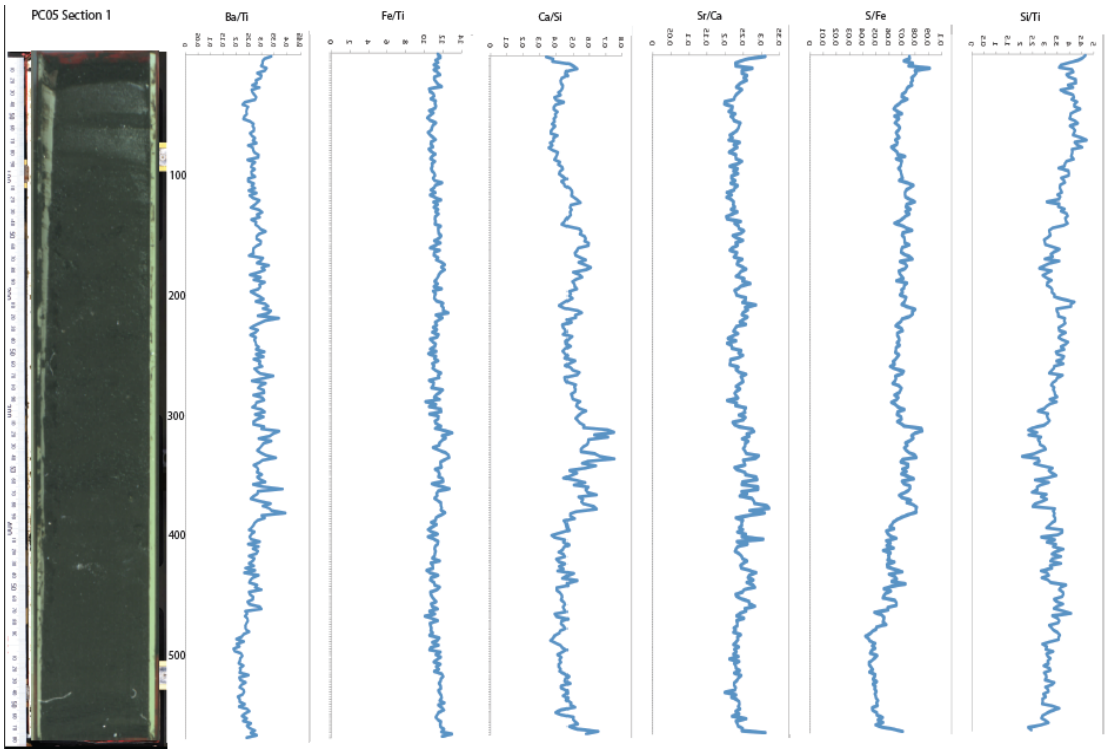

Figure 25. Core image and Ba/Ti, Fe/Ti, Ca/Si, Sr/Ca, S/Fe, and Si/Ti ratio plots for PC05 Section 1. Horizontal axes are the ratio values and vertical axes are depth down the core section in millimeters.

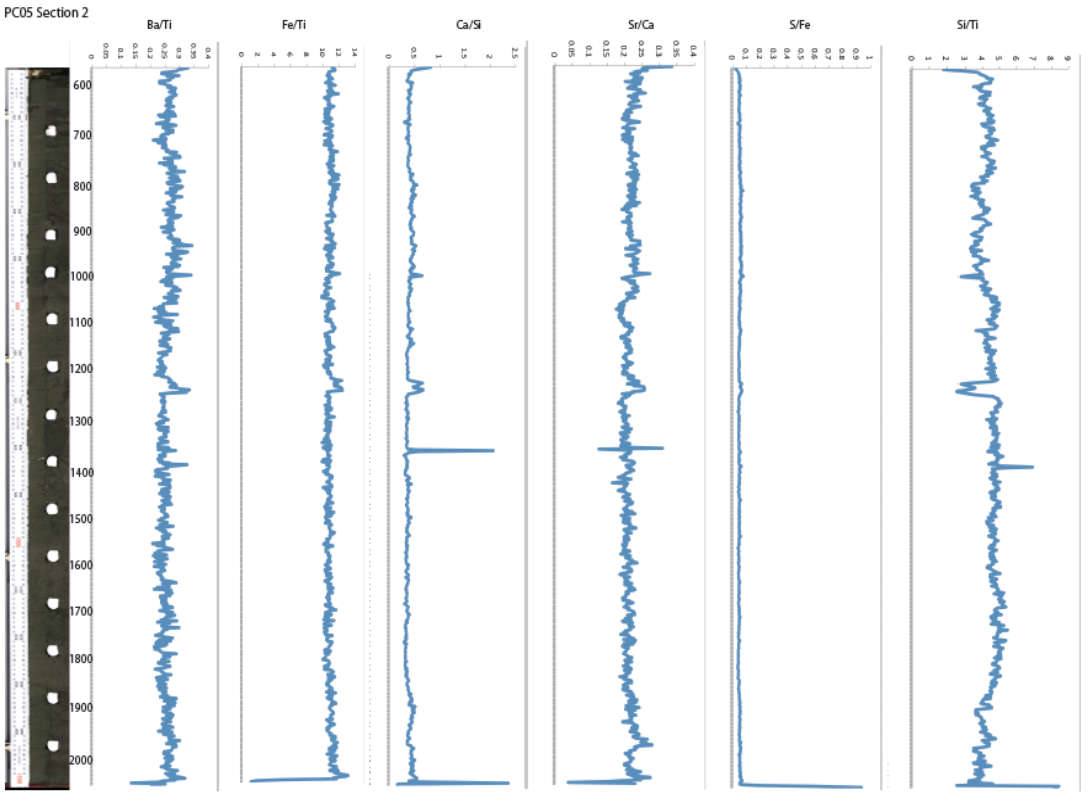

Figure 26. Core image and Ba/Ti, Fe/Ti, Ca/Si, Sr/Ca, S/Fe, and Si/Ti ratio plots for PC05 Section 2. Horizontal axes are the ratio values and vertical axes are depth down the core section in millimeters. This core has been sampled where white circles are seen.

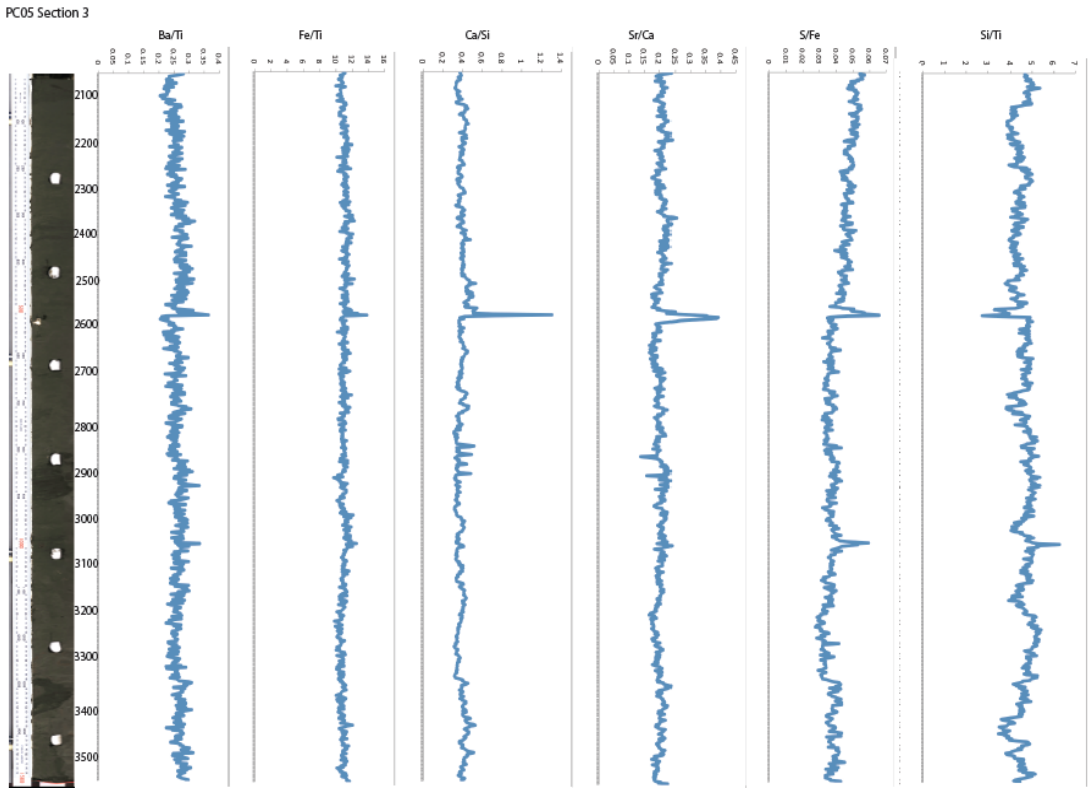

Figure 27. Core image and Ba/Ti, Fe/Ti, Ca/Si, Sr/Ca, S/Fe, and Si/Ti ratio plots for PC05 Section 3. Horizontal axes are the ratio values and vertical axes are depth down the core section in millimeters. This core has been sampled where white circles are seen.

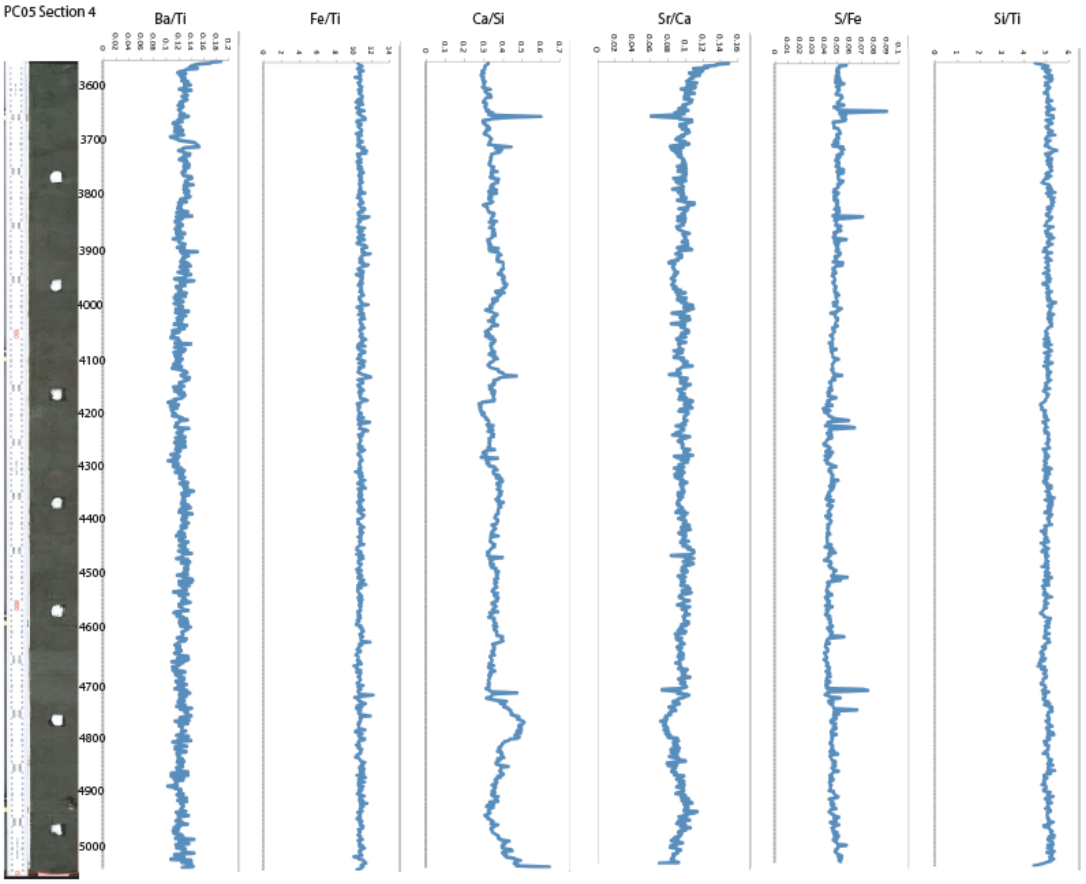

Figure 28. Core image and Ba/Ti, Fe/Ti, Ca/Si, Sr/Ca, S/Fe, and Si/Ti ratio plots for PC05 Section 4. Horizontal axes are the ratio values and vertical axes are depth down the core section in millimeters. This core has been sampled where white circles are seen.

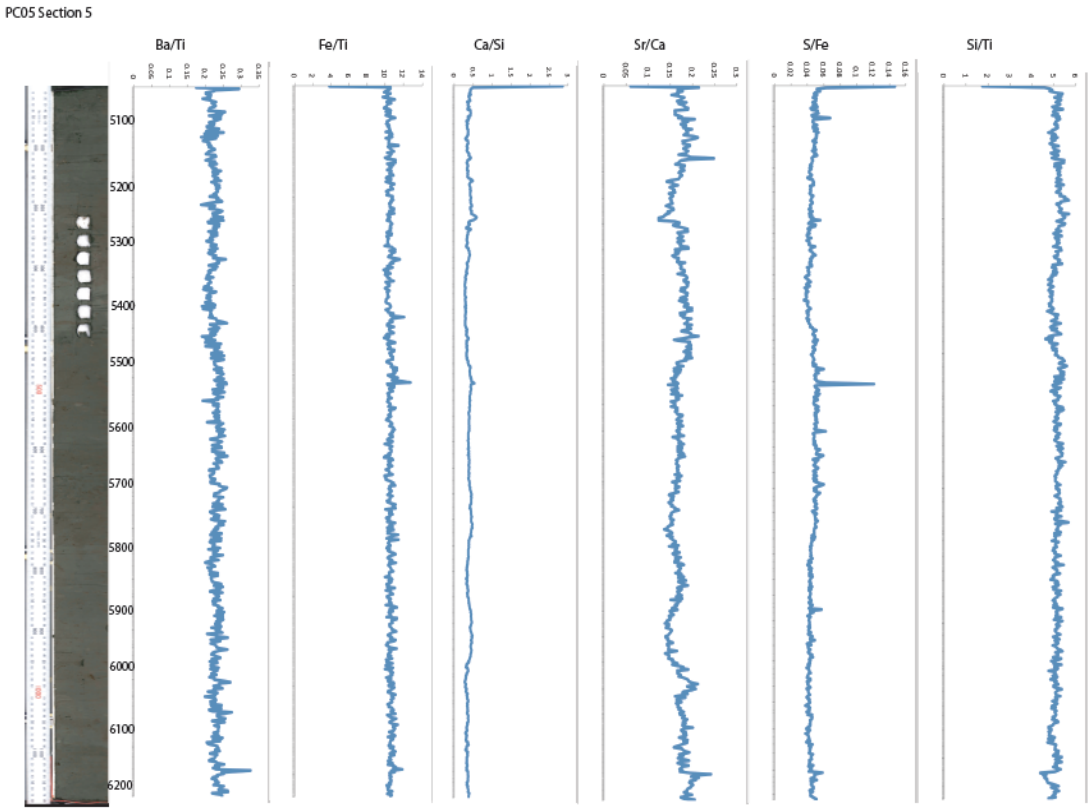

Figure 29. Core image and Ba/Ti, Fe/Ti, Ca/Si, Sr/Ca, S/Fe, and Si/Ti ratio plots for PC05 Section 5. Horizontal axes are the ratio values and vertical axes are depth down the core section in millimeters. This core has been sampled where white circles are seen.

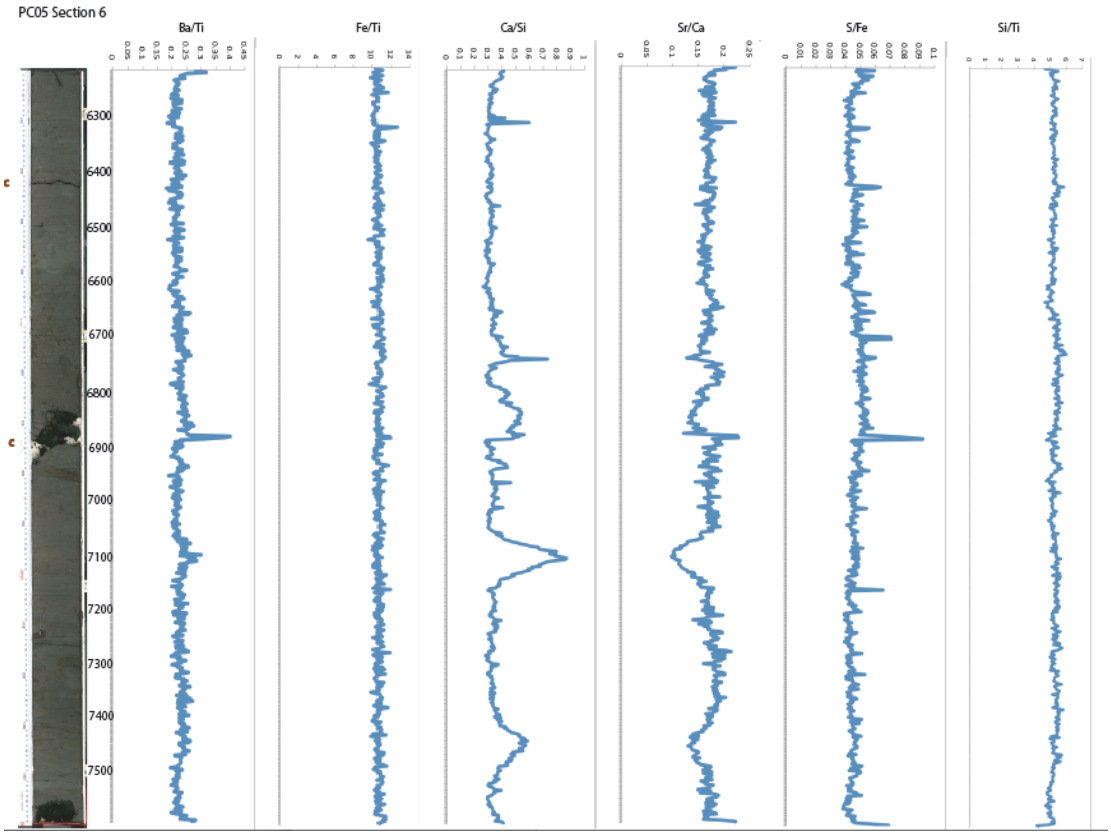

Figure 30. Core image and Ba/Ti, Fe/Ti, Ca/Si, Sr/Ca, S/Fe, and Si/Ti ratio plots for PC05 Section 6. Horizontal axes are the ratio values and vertical axes are depth down the core section in millimeters. Brown letters "c" show cracks in the sediments.

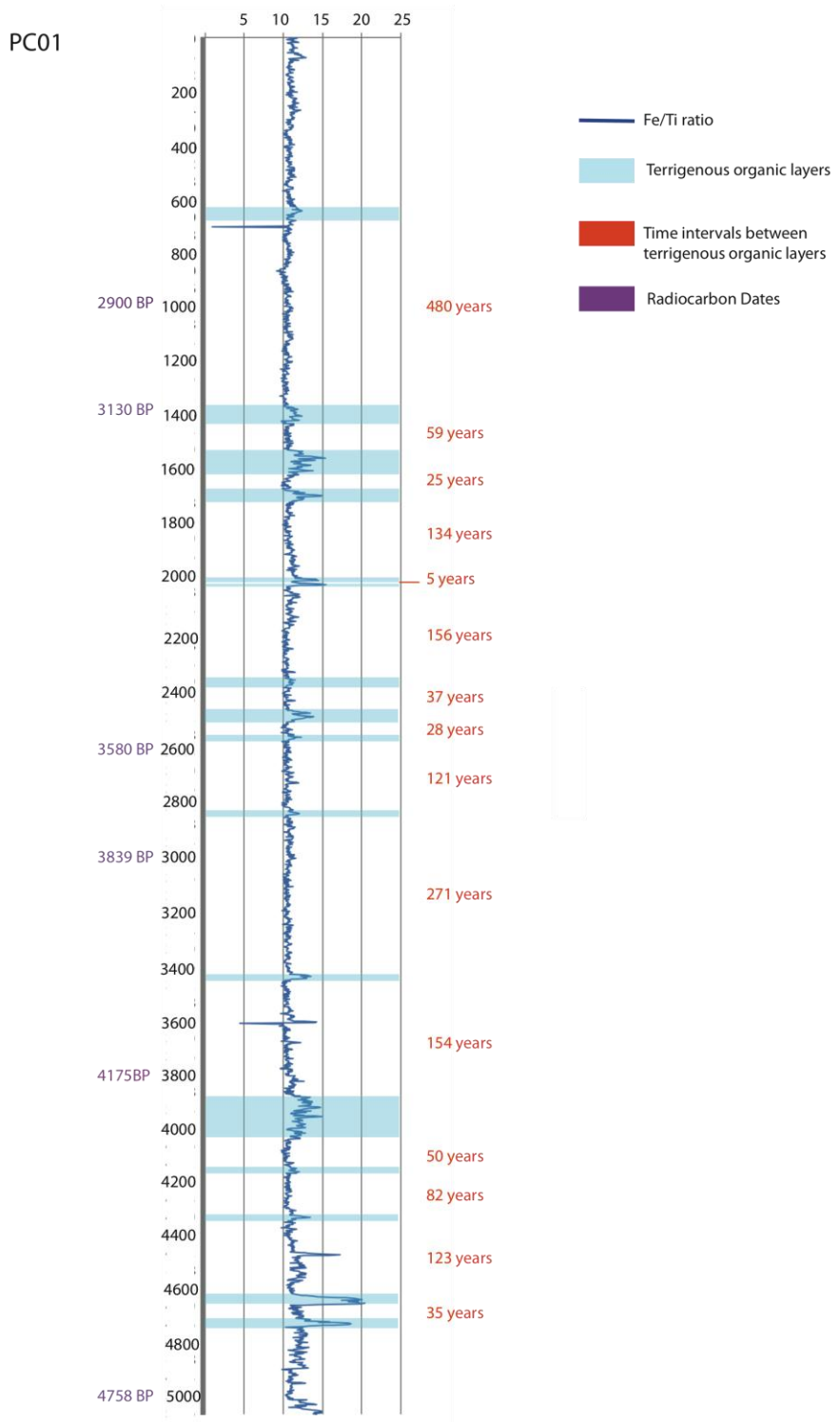

Figure 31. Calculated recurrence intervals (in orange) between the terrigenous organic layers for PC01. Fe/Ti ratio plotted for the whole PC01. Blue highlights indicate the depths at which organic layers are present. The vertical axis is the downcore depth in millimeters; the horizontal axis is the Fe/Ti ratio value. Purple dates are radiocarbon ages.

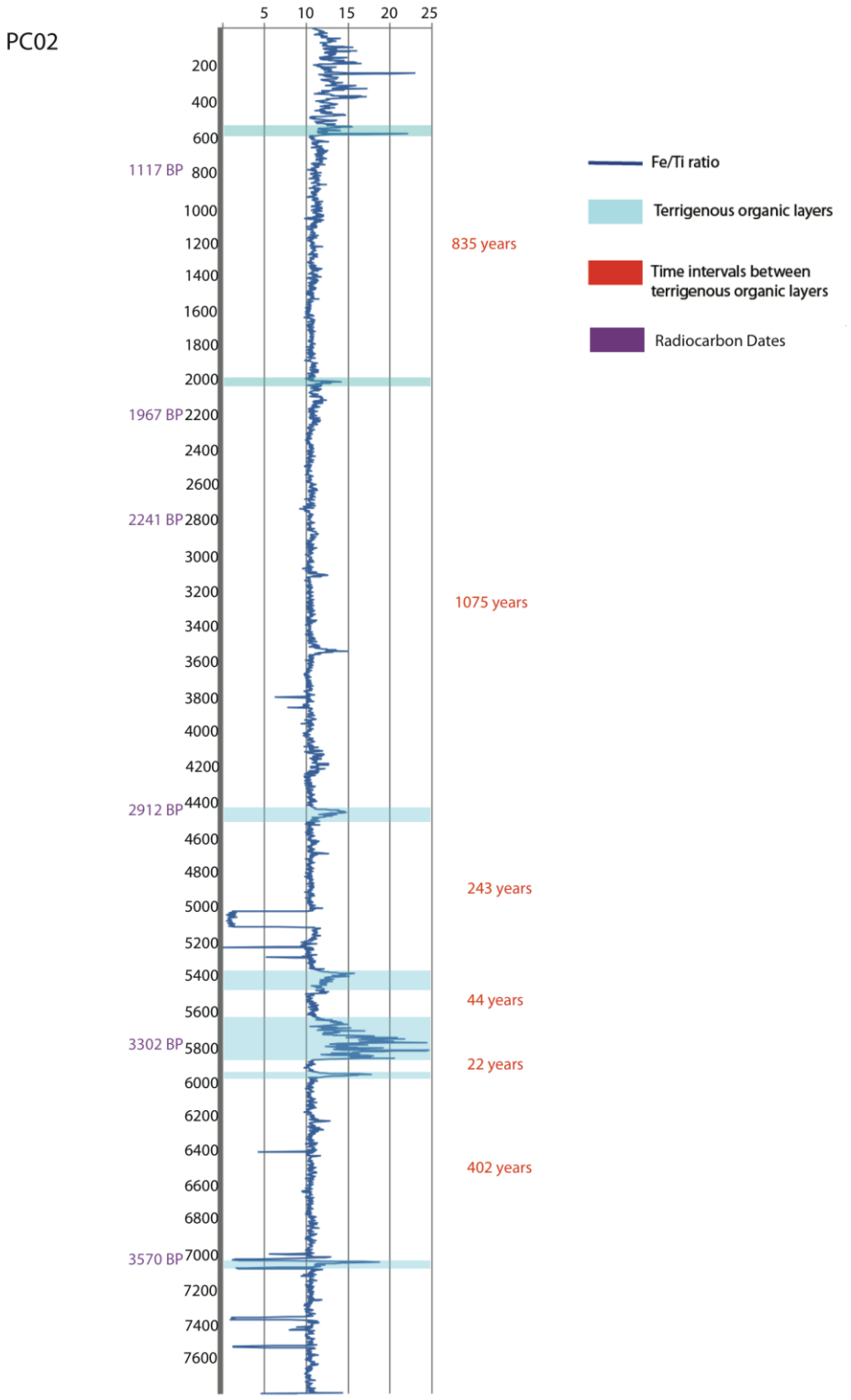

Figure 32. Calculated recurrence intervals (in orange) between the terrigenous organic layers for PC02. Fe/Ti ratio plotted for the whole PC02. Blue highlights indicate the depths at which organic layers are present. The vertical axis is the downcore depth in millimeters; the horizontal axis is the Fe/Ti ratio value. Purple dates are radiocarbon ages.

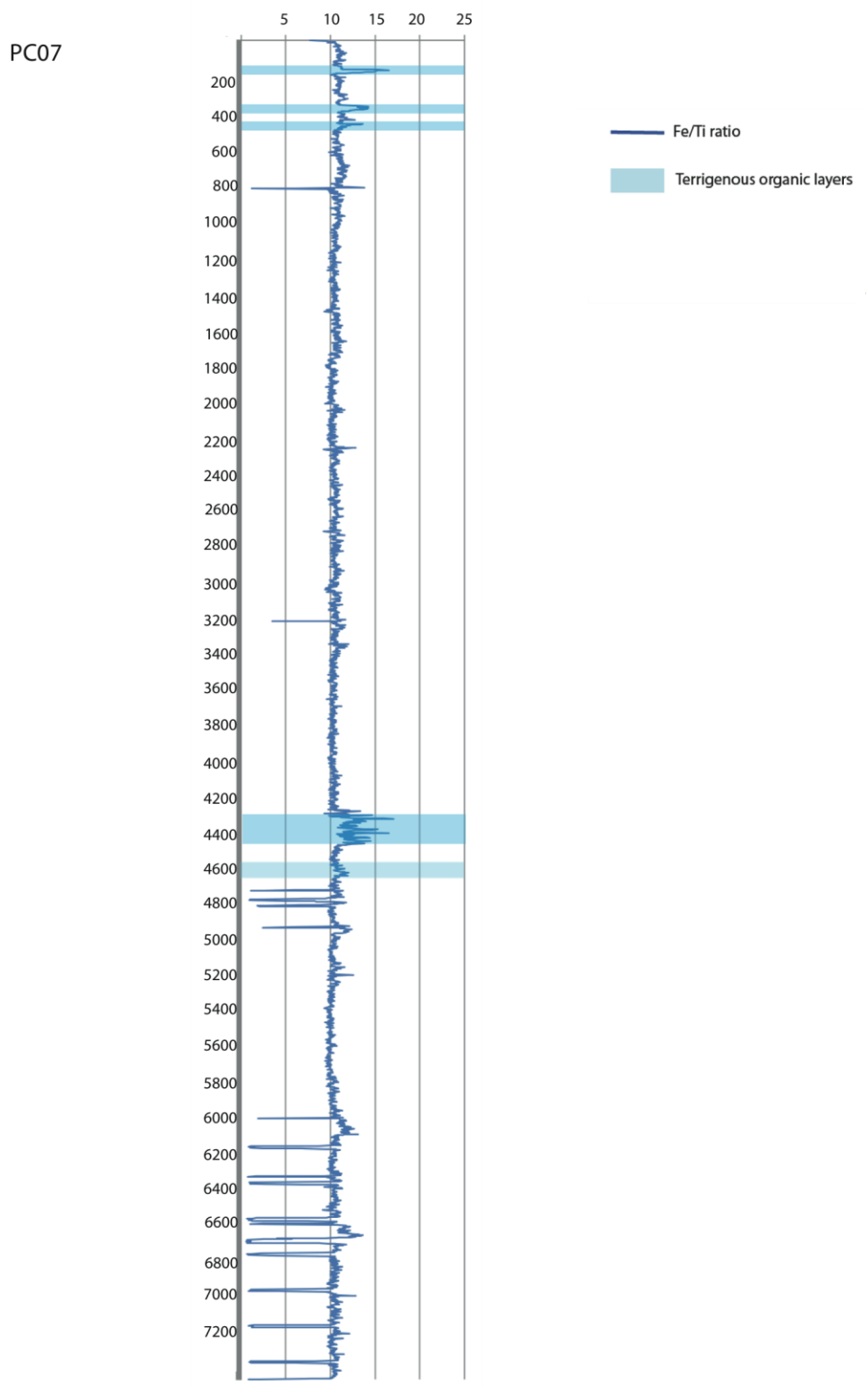

Figure 33. Fe/Ti ratio plotted for the whole PC07. The vertical axis is the downcore depth in millimeters; the horizontal axis is the Fe/Ti ratio value. Blue highlights indicate the depths at which organic layers are present. No dates are available for PC07.

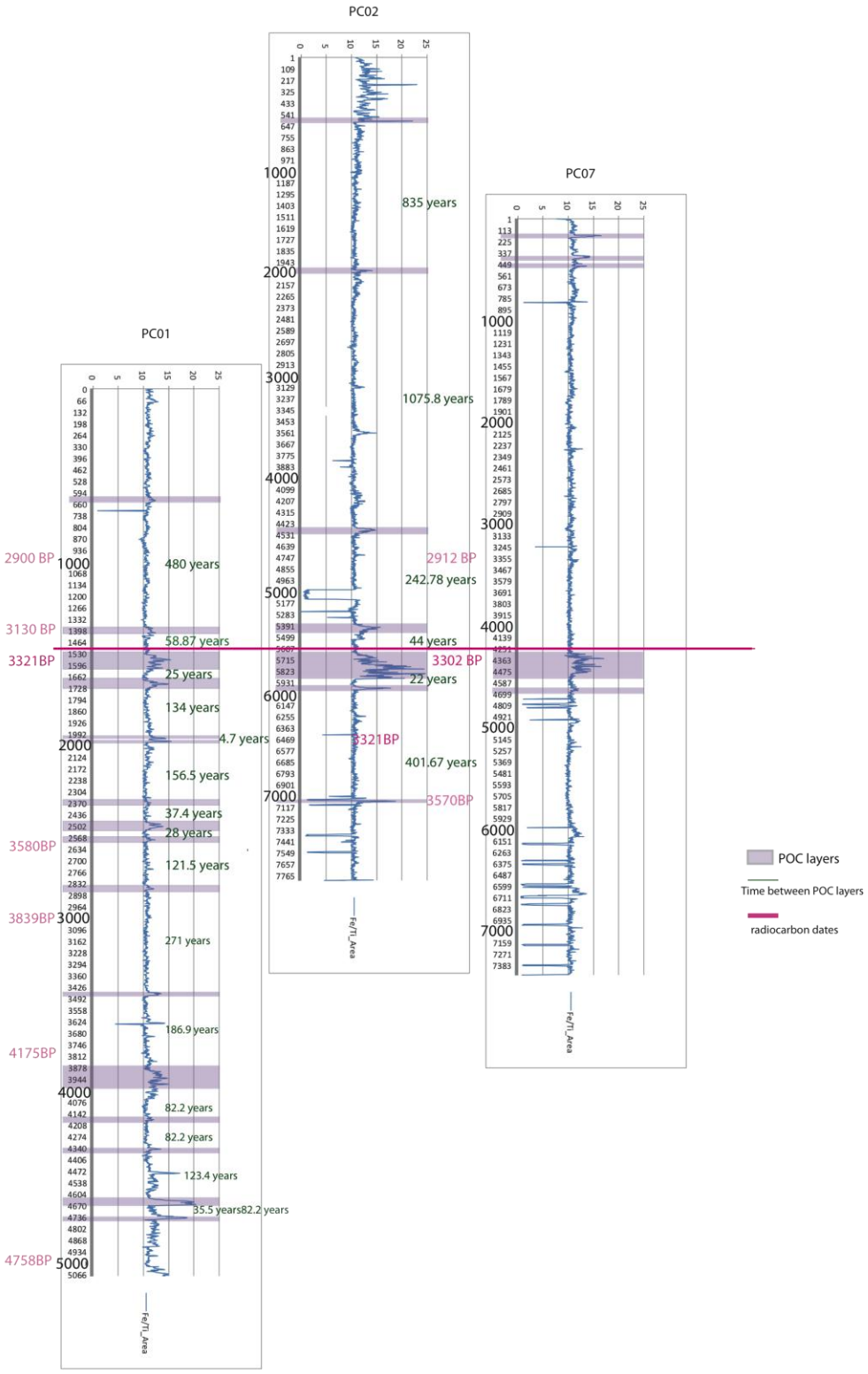

Figure 34. Tentative core correlation based on peak in Fe/Ti. Organic layers are labeled in purple. Recurrence intervals are indicated in green. Red dates indicate known radiocarbon ages for PC01 and PC02.

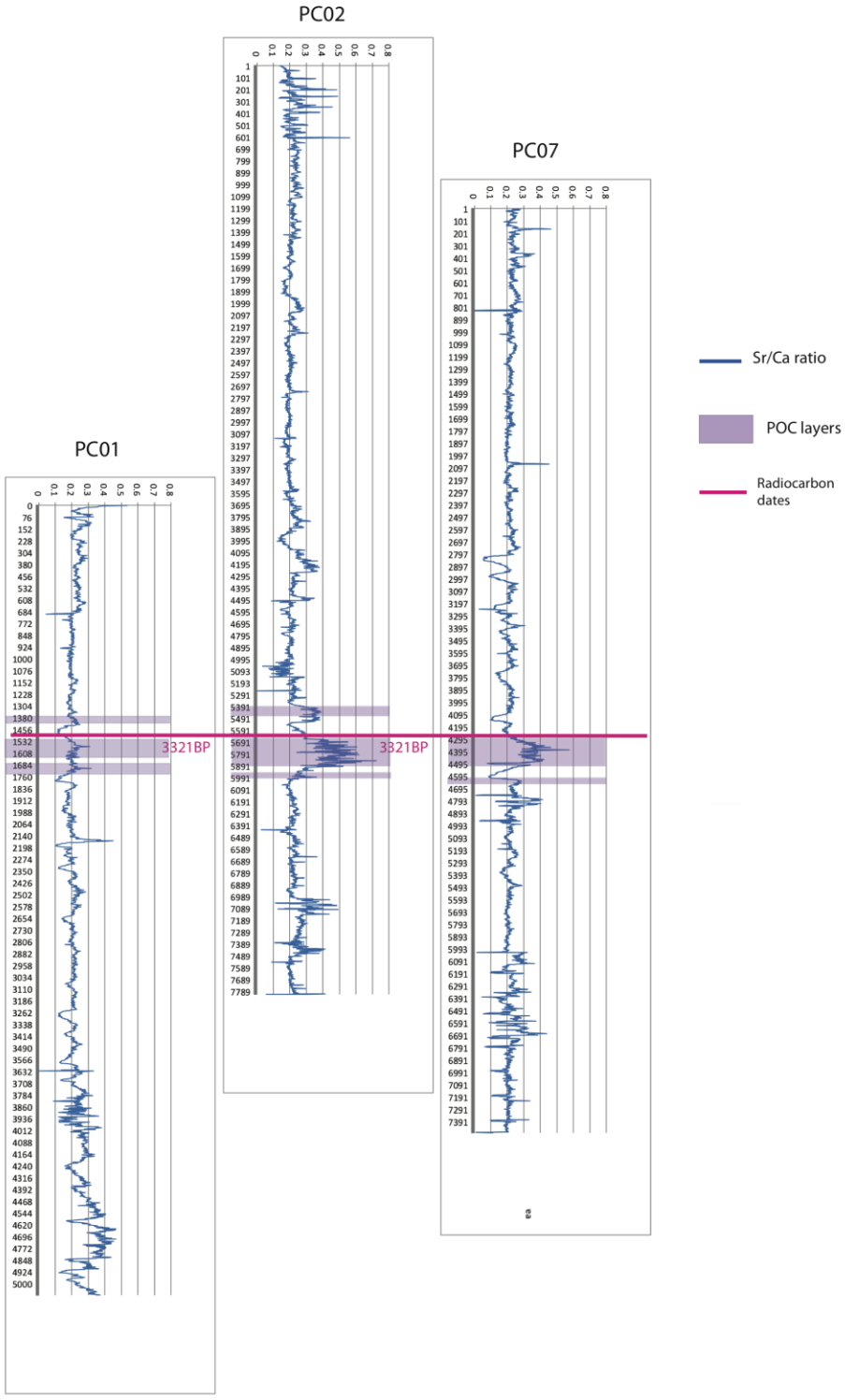

Figure 35. Tentative core correlation based on peak in Sr/Ca. Organic layers are labeled in purple. Red dates indicate known radiocarbon ages for PC01 and PC02.

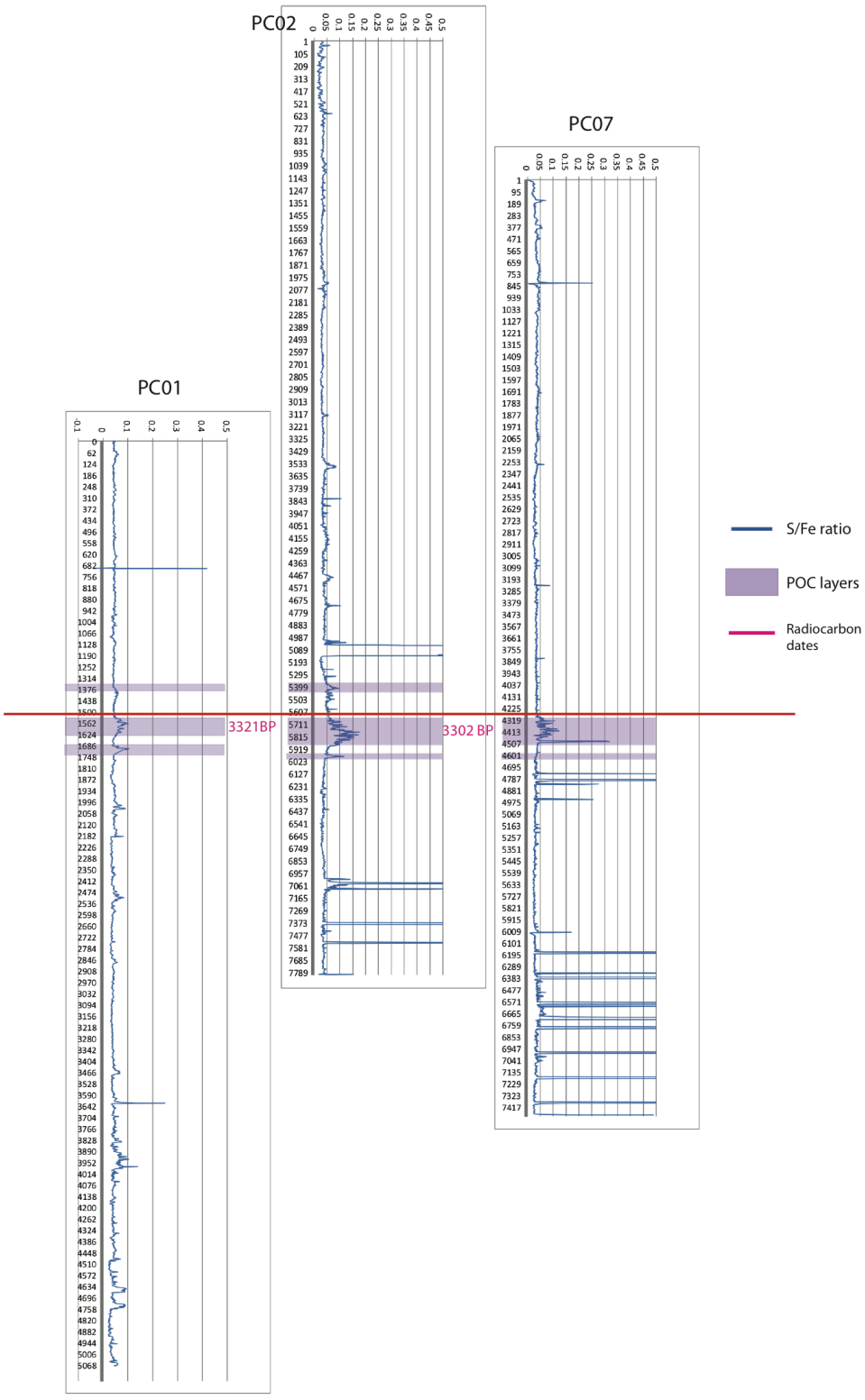

Figure 36. Tentative core correlation based on peak in S/Fe. Organic layers are labeled in purple. Red dates indicate known radiocarbon ages for PC01 and PC02.

Table 1. Coordinates and depth locations of the cores.

Core	Latitude	Longitude	Water Depth (m)	Length (m)
PC01	124°30'09.96" W	40°50'20.16" N	460	5.07
PC02	124°30'07.62" W	40°50'19.86" N	460	7.78
PC07	124°30'05.84" W	40°50'19.87" N	461	7.53
PC05	124°27'12.08" W	40°59'00.30" N	419	7.60

Table 2. The elements used as proxies, their atomic weights, and the concentration in ppm required for the Avaatech core scanner to detect them. The detection capability of the scanner generally increases with increasing atomic weight. Values from Richter et al., 2006.

Element	Atomic Weight	Avaatech Scanner Detection Limit (ppm)
Si	28	1000
S	32	500
Ti	48	500
Ca	40	200
Fe	56	45
Ba	137	40
Sr	88	5

Table 3. List of proxies and the information they convey.

Proxies	Indication	Signification
Ba/Ti	• Photic zone productivity indicator • Associated with the decomposition of organic material	• Increases in this ratio indicate the presence of organic material
Fe/Ti	• Terrigenous riverine input • Proxy for rainfall and flood events • Presence of pyrite and other sulfides	• Increases in the ratio indicate high organic content of the sediments
Ca/Si	• Allows to distinguish between sand of pelagic biogenic versus terrigenous origin	• Increases in the ratio indicate high calcium carbonate presence and thus pelagic deposition
Sr/Ca	• Allows to distinguish between sand of pelagic biogenic versus terrigenous origin	• Increases in the ratio indicate the dominance of terrigenous sand over biogenic sand
S/Fe	• Relative abundances of sulfides and sulfates • Sulfide: lowest oxidation state of sulfur. Reduced form of sulfur • Sulfate: Oxidized form of sulfur • In rapidly buried sediments, sulfate reduction rates are larger, making pyrite more abundant	• Pyrite, most common sulfide mineral. Strong positive correlation with organic carbon. Decreases in the ratio indicate the presence of sulfides • Sulfates: barite, gypsum. Byproducts of sulfide oxidation. Increases in the ratio indicate the presence of sulfates
Si/Ti	• Terrigenous riverine input • Proxy for rainfall and flood events	• Decreases in the ratio indicate high terrigenous content of the sediments

Table 4. Minimum, maximum, and average integral values per core section for Fe, Ti, Ba, Si, Ca, Sr, and S.

	Fe	Ti	Ba	Si	Ca	Sr	S
PC01 Sec1							
Minimum	40000	4000	1500	10000	8000	2000	2000
Maximum	160000	14000	4500	60000	25000	5000	7000
Average	80000	8000	2000	20000	12000	2500	5000
PC01 Sec2							
Minimum	6000	3000	1000	10000	10000	3500	3000
Maximum	140000	12000	8000	60000	45000	10000	8000
Average	120000	10000	4000	50000	20000	4000	5000
PC01 Sec3							
Minimum	100000	8000	Error	25000	20000	3000	3000
Maximum	140000	14000	Error	70000	60000	6000	8000
Average	120000	11000	Error	60000	30000	4000	4000
PC01 Sec4							
Minimum	20000	2000	500	10000	5000	1000	2000
Maximum	140000	14000	4000	60000	80000	13000	8000
Average	120000	10000	2700	50000	10000	4000	4000
PC02 Sec1							
Minimum	5000	2000	1000	10000	5000	1000	1000
Maximum	20000	16000	3500	50000	25000	4000	6000
Average	15000	14000	2700	30000	15000	3000	4000
PC02 Sec2							
Minimum	80000	8000	2500	10000	10000	2000	2000
Maximum	150000	14000	3500	60000	30000	5000	5000
Average	120000	10000	3000	40000	17000	4000	4000
PC02 Sec3							
Minimum	40000	4000	1500	10000	5000	2000	1000
Maximum	140000	13000	4000	70000	35000	7000	6000
Average	120000	12000	3500	50000	25000	4000	3000
PC02 Sec4							
Minimum	20000	2000	N/A	10000	2000	500	500
Maximum	150000	14000	N/A	70000	65000	6000	14000
Average	130000	12000	N/A	60000	20000	4000	5000
PC02 Sec5							
Minimum	40000	1000	200	3000	1000	200	500
Maximum	120000	12000	4000	70000	27000	4500	4500
Average	80000	8000	2000	50000	20000	3500	3500

Table 4. Minimum, maximum, and average integral values per core section for Fe, Ti, Ba, Si, Ca, Sr, and S, continued.

PC02 Sec6							
Minimum	10000	1500	500	5000	2000	200	1500
Maximum	140000	14000	4000	65000	30000	6000	12000
Average	120000	10000	3500	35000	20000	4000	6000
PC02 Sec7							
Minimum	20000	4000	500	10000	5000	1000	1000
Maximum	140000	14000	4000	70000	35000	5000	12000
Average	120000	12000	3500	60000	20000	4000	4000
PC07 Sec1							
Minimum	20000	2000	500	10000	5000	1000	1000
Maximum	160000	14000	3500	50000	20000	5000	6000
Average	120000	10000	3000	30000	15000	3500	4000
PC07 Sec2							
Minimum	50000	5000	2000	20000	10000	3000	4000
Maximum	120000	13000	4500	60000	30000	5000	6000
Average	120000	12000	3250	45000	20000	4700	5000
PC07 Sec3							
Minimum	20000	4000	1500	10000	5000	2000	1000
Maximum	140000	14000	4000	70000	140000	8000	7000
Average	120000	12000	3500	60000	20000	4000	4500
PC07 Sec4							
Minimum	20000	4000	500	10000	10000	2000	1000
Maximum	140000	13000	3700	60000	50000	6000	25000
Average	120000	12000	3500	50000	20000	4000	5000
PC07 Sec5&6							
Minimum	60000	2000	100	2000	2000	200	500
Maximum	150000	15000	4000	70000	40000	5000	13000
Average	120000	14000	3500	70000	20000	4500	4000
PC07 Sec7							
Minimum	500	600	400	3000	700	60	400
Maximum	160000	145000	4300	74000	140000	8000	11000
Average	140000	11000	3000	15000	17000	4000	4000
PC05 Sec1							
Minimum	50000	4000	1300	10000	6000	1500	3000
Maximum	100000	9000	2000	35000	14000	3000	6000
Average	80000	7000	1800	22000	11000	2500	5000
PC05 Sec2							
Minimum	50000	5000	1300	10000	10000	2000	1000

Table 4. Minimum, maximum, and average integral values per core section for Fe, Ti, Ba, Si, Ca, Sr, and S, continued.

Maximum	100000	9000	2300	40000	60000 (shell)	8000	6000
Average	80000	8000	2000	35000	10000	2200	4000
PC05 Sec3							
Minimum	30000 (shell)	3000 (shell)	1000	10000	4000	1000	1500
Maximum	90000	8500	2500	45000	16000	5500	4000
Average	70000	7500	2000	30000	12000	2500	3500
PC05 Sec4							
Minimum	100000	10000	1500	40000	15000	1500	5000
Maximum	200000	18000	2500	90000	45000	3500	16000
Average	150000	16000	2000	85000	25000	3000	8000
PC05 Sec5							
Minimum	20000	4000	1000	10000	10000	1500	3000
Maximum	110000	10000	2300	50000	35000	4500	12000
Average	100000	9000	2000	50000	30000	3000	4200
PC05 Sec6							
Minimum	20000	2000	600	10000	5000	1000	2000
Maximum	100000	10000	2200	50000	30000	4500	6000
Average	90000	8000	1700	45000	15000	2500	4000

Table 5. Minimum, maximum, and average ratio values per core section for Ba/Ti, Fe/Ti, Ca/Si, Sr/Ca, S/Fe, Si/Ti.

	Ba/Ti	Fe/Ti	Ca/Si	Sr/Ca	S/Fe	Si/Ti
PC01 Sec1						
Minimum	0.25	10	0.3	0.1	0.03	1.5
Maximum	0.5	14	1	0.55	0.06	4.5
Average	0.35	11	0.6	0.3	0.04	3.5
PC01 Sec2						
Minimum	0.3	10	0.5	0.05	0.05	2
Maximum	1.6	16	3.5	0.4	0.15	5
Average	0.4	11	0.5	0.2	0.05	4.5
PC01 Sec3						
Minimum	0.002 (error)	10	0.5	0.1	0.03	3
Maximum	0.012 (error)	14	2	0.3	0.15	6
Average	0.006 (error)	10	0.5	0.2	0.05	5
PC01 Sec4						
Minimum	0.2	9	0.25	0.1	0.02	2
Maximum	0.45	17	3	0.4	0.14	7
Average	0.35	10	0.5	0.25	0.04	5
PC02 Sec1						
Minimum	0.15	10	0.3	0.1	0.02	1
Maximum	0.6	22	1.2	0.5	0.06	3.5
Average	0.25	14	0.7	0.3	0.03	2
PC02 Sec2						
Minimum	0.2	9	0.2	0.2	0.02	2
Maximum	0.4	14	0.8	0.3	0.06	5
Average	0.3	11	0.4	0.25	0.04	4
PC02 Sec3						
Minimum	0.2	9	0.3	0.1	0.02	2
Maximum	0.3	14	1.2	0.2	0.05	5
Average	0.45	11	0.4	0.3	0.04	5
PC02 Sec4						
Minimum	N/A	4	0.25	0.1	0.04	3

Table 5. Minimum, maximum, and average ratio values per core section for Ba/Ti, Fe/Ti, Ca/Si, Sr/Ca, S/Fe, Si/Ti, continued.

Maximum	N/A	14	1.5	0.35	0.1	7
Average	N/A	10	0.5	0.2	0.05	5
PC02 Sec5						
Minimum	0.1	2	0.2	0.05	0.2	2
Maximum	0.4	12	0.5	0.3	1.8	6
Average	0.25	10	0.35	0.2	1	4
PC02 Sec6						
Minimum	0.1	5	0.25	0.1	0.02	2
Maximum	0.5	25	1	0.7	0.18	6
Average	0.2	10	0.5	0.3	0.04	4
PC02 Sec7						
Minimum	0.1	2	0.25	0.1	0.05	3
Maximum	0.5	18	0.6	0.5	1	6.7
Average	0.3	10	0.5	0.2	0.05	5
PC07 Sec1						
Minimum	0.2	8	0.5	0.15	0.03	1
Maximum	0.5	16	1.5	0.45	0.1	4
Average	0.2	10	0.5	0.25	0.04	3
PC07 Sec2						
Minimum	0.2	9	0.3	0.15	0.02	3
Maximum	0.4	11	0.6	0.3	0.05	5
Average	0.3	10	0.4	0.22	0.04	4
PC07 Sec3						
Minimum	0.2	9	0.5	0.05	0.03	3
Maximum	0.45	12	3	0.45	0.07	5
Average	0.3	10	0.5	0.2	0.04	4.5
PC07 Sec4						
Minimum	0.15	10	0.5	0.1	0.04	3
Maximum	0.4	17	2	0.5	0.3	6.5
Average	0.25	10	0.75	0.2	0.05	5

Table 5. Minimum, maximum, and average ratio values per core section for Ba/Ti, Fe/Ti, Ca/Si, Sr/Ca, S/Fe, Si/Ti, continued.

PC 07 Sec5&6						
Minimum	0.1	1	0.2	0.05	0.05	2
Maximum	0.65	13	2	0.4	0.9	6
Average	0.2	10	0.4	0.2	0.05	5
PC07 Sec7						
Minimum	0.08	0.6	0.2	0.01	0.01	2
Maximum	0.5	14	4	0.4	1.7	7
Average	0.3	10	0.3	0.2	0.1	5
PC05 Sec1						
Minimum	0.2	10	0.3	0.2	0.04	2
Maximum	0.35	13	0.75	0.3	0.09	4.5
Average	0.25	11	0.5	0.25	0.065	3.5
PC05 Sec2						
Minimum	0.2	10	0.3	0.15	0.1	2
Maximum	0.35	14	2 (shell)	0.35	0.1	7
Average	0.25	13	0.5	0.25	0.1	4
PC05 Sec3						
Minimum	0.15	8	0.2	0.1	??0.01	2
Maximum	0.4	14	1.2	0.4	??0.06	6.5
Average	0.25	11	0.4	0.2	0.04	4.5
PC05 Sec4						
Minimum	0.1	10	0.2	0.04	0.03	4.5
Maximum	0.2	12	0.6	0.15	0.09	5
Average	0.13	11	0.3	0.1	0.05	5
PC05 Sec5						
Minimum	0.15	4	0.25	0.05	0.04	2
Maximum	0.3	13	1	0.25	0.12	6
Average	0.25	11	0.5	0.15	0.05	5
PC05 Sec6						
Minimum	0.2	10	0.3	0.1	0.03	4.5
Maximum	0.35	13	0.9	0.25	0.09	5.5
Average	0.25	11	0.4	0.2	0.05	5

Bibliography

Alexander, C. R. & Simoneau, A. M., 1999. Spatial variability in sedimentary processes on the Eel continental slope. Marine Geology **154**, 243-245.

Aller, R. C. & Rude, P. D., 1987. Complete oxidation of solid phase sulfides by manganese and bacteria in anoxic marine sediments. Geochimica et Cosmochimica Acta **52**, 731-765.

Barnard, P. L. & Warrick, J. A., 2010. Dramatic beach and nearshore morphological changes due to extreme flooding at a wave-dominated river mouth. Marine Geology **271**, 131-148.

Berner, R. A. & Raiswell, R., 1983. Burial of organic carbon and pyrite sulfur in sediments over Phanerozoic time: a new theory. Geochemica et Cosmochimica Acta **47**, 855-862.

Burger R. L., Fulthorpe, C. S., Austin, J. A. Jr, 2001. Late Pleistocene channel incision in the southern Eel River Basin, northern California: implications for tectonic vs. eustatic influences on shelf sedimentation patterns. Marine Geology **177**, 317-330.

Cacchione, D. A., Wiberg, P.L., Lynch, J., Irish, J., Traykovski, P., 1999. Estimates of suspended-sediment flux and bedform activity on the inner portion of the Eel continental shelf. Marine Geology **154**, 83-97.

Canfield, D. E., 1993. Organic matter oxidation in sediments. In: Wollast, R., Chou, L., Mackenzie, F. (Eds.). Interactions of C, N, P and S Biochemical Cycles. NATO ASI Series, Springer, Berlin, pp. 333-363.

Chao, Y., Ghil, M., McWilliams, J. C., 2000. Pacific interdecadal variability in this century's sea surface temperatures. Geophysical Research Letters **27**, 2261–2264.

Croudace, I. W., Rindby, A., Rothwell, R. G., 2006. ITRAX: description and evaluation of a new multi-function X-ray core scanner. In: Rothwell, R. G. (Ed.), *New techniques in sediment core analysis*. Geological Society, London, Special Publications **267**, 51-63.

Drake, D. E., 1999. Temporal and spatial variability of the sediment grain-size Distribution on the Eel shelf: the flood layer of 1995. Marine Geology **154**, 160-182.

Driscoll, N. W., Weissel, J. K., Goff, J. A., 2000. Potential for large-scale submarine slope failure and tsunami generation along the U.S. mid Atlantic coast. Geology **28**, 407-410.

Francois, R., Honjo, S., Manganini, S.J., Ravizza, G.E., 1995. Biogenic barium fluxes to the deep sea: implications for paleoproductivity reconstructions. Global Biogeochemistry. Cycles 9, 289-303.

Gedalof, Z., Mantua, N. J., Peterson, D. L., 2002. A multi-century perspective of Variability in the Pacific Decadal Oscillation: new insights from tree rings and Coral. Geophysical Research Letters **29**, 57.

Govil, P., Naidu, P. D., Radhika, T. K., 2004. Major turbidity flows in the Western Indus Fan between 290 and 360 kyr. Current Science **87**, 1597-1599.

Gulick, S. P. S., Meltzer , A. S., Clarke, S. H. Jr., 2002. Effect of the northward migrating Mendocino triple junction on the Eel River forearc basin, California: Stratigraphic development. GSA Bulletin **114**, 178-191.

Harris, P. T., Baker, E. K., Cole, A. R., Short, S. A., 1993. A preliminary study of sedimentation in the tidally dominated Fly River Delta, Gulf of Papua. Continental Shelf Research **13**, 441-472.

Haschke, M., 2006. The Eagle III BKA system, a novel sediment core X-ray fluorescence analyzer with very high spatial resolution. In: Rothwell, R. G. (Ed.), *New techniques in sediment core analysis*. Geological Society, London, Special Publications **267**, 31-37.

Haug, G. H., Hughen, K. A., Sigman, D. M., Peterson, L. C., Röhl, U., 2001. Southward migration of the Intertropical Convergence Zone through the Holocene. Science **293**, 1304-1308.

Hedges, J. I. & Keil, R. G., 1995. Sedimentary organic matter preservation: an assessment and speculative synthesis. Marine Chemistry **49**, 81-115.

Hughen, K. A., Baillie, M. G. L., Bard, E., Beck, J. W., Bertrand, C. J. H., Blackwell, P. G., Buck, C. E., Burr, G.S., Cutler, K. B., Damon, P.E., Edwards, R. L., Fairbanks, R. G., Friedrich, M., Guilderson, T. P., Kromer, B., McCormac, G., Manning, S., Ramsey, C. B., Reimer, P., Reimer, R. W., Remmele, S., Southon, J. R., Stuiver, M., Talamo, S., Taylor, F. W., van der Plicht, J., Weyhenmeyer, C. E., 2004. Marine04 marine radiocarbon age calibration, 0-26 cal kyr BP. Radiocarbon **46**, 1059–1086.

Ingram, B. L. and Sloan, D., 1992. Strontium isotopic composition of estuarine sediments as paleosalinity-paleoclimate indicator. Science **255**, 68-72.

Jenkins, R. & De Vries, J. L., 1970. Practical X-Ray Spectrometry. Macmillan, London.

Jørgensen, B.B., 1982. Mineralization of organic matter in the sea bed: The role of sulfate reduction. Nature **296**, 643–645.

Lee, H., Locat, J., Dartnell, P., Israel, K., Wong, F., 1999. Regional variability of slope stability: application to the Eel margin, California. Marine Geology **154**, 305-321.

Lee, H. J., Syvitski, J. P. M., Parker, G., Orange, D., Locat, J., Hutton, E. W. H., Imran, J., 2002. Distinguishing sediment waves from slope failure deposits: field Examples, including the "Humboldt Slide", and modeling results. Marine Geology **192**, 79-104.

Ludwig, W., Probst, J-l., Kempe, S., 1996. Predicting the oceanic input of organic Carbon by continental erosion. Global Biogeochemical Cycles **10**, 23-41.

MacDonald, G. M. & Case, R. A., 2005. Variations in the Pacific Decadal Oscillation over the past millennium. Geophysical Research Letters **32**, L08703.

Mantua, N. J., Hare, S. R., Zhang, Y., Wallace, J. M., Francis, R. C., 1997. A Pacific interdecadal climate oscillation with impacts on salmon production. Bulletin of the American Meteorological Society **78**, 1069-1079.

Mantua, N. J. & Hare, S.R., 2002. The Pacific Decadal Oscillation. Journal of Oceanography **58**, 35-44.

Martin, J. H., Gordon R. M., S. Fitzwater and W. W. Broenkow (1989): VERTEX: phytoplankton/iron studies in the Gulf of Alaska. Deep-Sea Research **36**, 649-680.

McCullough, J. S., 2009. The Importance of Landslides and Flooding Events in Harvesting and Sequestering Macroscopic Carbon along Active Margins: The Eel Basin, Northern California. Master's Thesis, University of California, San Diego.

McManus, J., Berelson, W. M., Klinkhammer, G. P., Johnson, K. S., Coale, K. H., Anderson, R. F., Kumar, N., Burdige, D. J., Hammond, D. E., Brumsack, H. J., McCorkle, D. C., Rushdi, A. 1998. Geochemistry of Barium in marine

sediments: implications for its use as a paleoproxy. Geochemica et Cosmochimica **62**, 3453-3473.

Milliman, J. D. & Meade, R. H., 1983. World-wide delivery of river sediment to the Oceans. Journal of Geology **91**, 1–21.

Milliman, J. D. & Syvitski, P. M., 1992. Geomorphic/tectonic control of sediment transport to the ocean: the importance of small mountainous rivers. Journal of Geology **100**, 525– 544.

Minobe, S., 2000. Spatio-temporal structure of the pentadecadal variability over the North Pacific. Progress in Oceanography **47**, 381–408.

Minobe, S., Jin, F. F., 2004. Generation of interannual and interdecadal climate Oscillations through nonlinear subharmonic resonance in delayed Oscillators. Geophysical Research Letters **31**, L16206.

Morehead, M. & Syvitski, J., 1998. River-plume sedimentation modeling for sequence stratigraphy: application to the Eel margin, northern California. Marine Geology, **154**, 29-41.

Newman, K. R., Cormier, M. H., Weissel, J. K., Driscoll, N. W., Kastner, M., Solomon, E. A., Robertson, G., Hill J. C., Singh H., Camilli, R., Eustice, R., 2008. Active methane venting observed at giant pockmarks along the U.S. mid-Atlantic shelf break. Earth and Planetary Science Letters **267**, 341-352.

Nittrouer, C. A., 1998. STRATAFORM: overview of its design and synthesis of its results. Marine Geology **154**, 3-12.

Paytan, A., Kastner, M., Chavez, F. P., 1996. Glacial and interglacial fluctuations in productivity in the Equatorial Pacific as indicated by marine barite. Science **274**, 1355-1357.

Pfeifer, K., Kasten, S., Hensen, C., Schulz, H. D., 2001. Reconstruction of primary productivity from the barium contents in surface sediments of the South Atlantic Ocean. Marine Geology, **177**, 13-24.

Puig, P., Ogston, A.S., Mullenbach, B.L., Nittrouer, C.A., Sternberg, R.W., 2003. Shelf-to-canyon sediment-transport processes on the Eel continental margin (northern California). Marine Geology **193**, 129-149.

Qiu, B., Schneider, N., Chen, S., 2006. Coupled Decadal Variability in the North Pacific: An Observationally Constrained Idealized Model. Journal of Climate **20**, 3602-3619.

Reitz, A., Pfeifer, K., de Lange, G. J., Klump, J., 2004. Biogenic barium and the detrital Ba/Al ratio: a comparison of the direct and indirect determination. Marine Geology **204**, 289-300.

Revel, M., Ducassou, E., Grousset, F.E., Bernasconi, S.M., Migeon, S., Revillon, S., Mascle, J., Murat, A., Zaragosi, S., Bosch, D., 2010. 100,000 Years of African monsoon variability recorded in sediments of the Nile margin. Quaternary Science Reviews **29**, 1342-1362.

Richter, T. O., Van Der Gaast, S., Koster, B., Vaars, A., Gieles, R., De Stigter, H. C., De Haas, H., Van Weering, T. C. E., 2006. The Avaatech XRF core scanner: technical description and applications to NE Atlantic sediments. In: Rothwell, R. G. (Ed.), *New techniques in sediment core analysis*. Geological Society, London, Special Publications **267**, 39-50.

Rothwell, R. G., Hoogakker, B., Thomson, J., Croudace, I. W., Frenz, M., 2006. Turbidite emplacement on the southern Balearic Abyssal Plain (western Mediterranean Sea) during Marine Isotope Stages 1-3: an application of ITRAX XRF scanning of sediment cores of lithostratigraphic analysis. In: Rothwell, R. G. (Ed.), *New techniques in sediment core analysis*. Geological Society, London, Special Publications **267**, 79-98.

Rothwell, R. G., & Rack, F.R., 2006. New techniques in sediment core analysis: an introduction. In: Rothwell, R. G. (Ed.), *New techniques in sediment core analysis*. Geological Society, London, Special Publications **267**, 1-29.

Schwehr, K., Driscoll, N., Tauxe, L., 2007. Origin of continental margin morphology: Submarine-slide or downslope current-controlled bedforms, a rock manetic approach. Marine Geology **240**, 19-41.

Sommerfield, C. K. & Nittrouer, C. A., 1997. Modern accumulation rates and a sediment budget for the Eel shelf: a flood-dominated depositional environment. Marine Geology **154**, 227-241.

Spinelli, G. A. & Field, M. E., 2003. Controls of tectonic and sediment source locations on along-strike variations in transgressive deposits on the northern California margin. Marine Geology **197**, 35-47.

Syvitski, J. P., Morehead, M. D., 1999. Estimating river-sediment discharge to the ocean: application to the Eel margin, northern California. Marine Geology **154**, 13-28.

Thomson, J., Croudace, I. W., Rothwell, R. G., 2006. A geochemical application of the ITRAX scanner to a sediment core containing eastern Mediterranean sapropel units. In: Rothwell, R. G. (Ed.), *New techniques in sediment core analysis*. Geological Society, London, Special Publications **267**, 65-77.

Tourre, Y. M., Rajagopalan, B., Kushnir, Y., Barlow, M., White, W. B., 2001. Patterns of coherent decadal and interdecadal climate signals in the Pacific Basin during the 20th century. Geophysical Research Letters **28**, 2069-2072.

Unruh, J., Humphrey, J., Barron, A., 2003. Transtensional model for the Sierra Nevada frontal fault system, eastern California. Geology **31**, 327-330.

Walsh, J. P. & Nittrouer, C. A., 1998. Observations of sediment flux to the Eel continental Slope, northern California. Marine Geology **154**, 55-68.

Warrick, J. A. & Milliman J.D., 2003. Hyperpycnal sediment discharge from Semiarid southern California rivers: Implications for sediment coastal budgets. Geology **31**, 781-784.

Warrick, J. A., Mertes, L. A. K., Washburn, L., Siegel, D. A., 2004. Dispersal forcing of southern California river plumes, based on field and remote sensing observations. Geo-Marine Letters **24**, 46-52.

Warrick, J. A., DiGiacomo, P. M., Weisberg, S. B., Nezlin, N.P., Mengel, M., Jones, B.H., Ohlmann, J. C., Washburn, L., Terrill, E. J., Farnsworth, K. L., 2007. River plume patterns and dynamics within the Southern California Bight. Continental Shelf Research **27**, 2427-2448.

Wells, M. L., Price, N. M., Bruland, K. W., 1995. Iron chemistry in seawater and its relationship to phytoplankton: a workshop report. Marine Chemistry **48**, 157-182.

Wheatcroft, R. A., Sommerfield, C. K., Drake, D. E., Borgeld, J. C., Nittrouer, C. A., 1997. Rapid and widespread dispersal of flood sediment on the Northern California margin. Geology **25**, 163-166.

Yarincik, K. M., Murray, R. W., Peterson, L.C., 2000. Climatically sensitive eolian and hemipelagic deposition in the Cariaco Basin, Venezuela, over the past 578,000 years: Results from AI/Ti and K/AI. Paleoceanography **15**, 210-228.